Post-print of
https://doi.org/10.1029/2018JB016708

Fracture Mechanical Properties of Damaged and Hydrothermally Altered Rocks, Dixie Valley - Stillwater Fault Zone, Nevada, USA

Owen A. Callahan[1*], Peter Eichhubl[1], Jon E. Olson[2], and Nicholas C. Davatzes[3]

[1]Bureau of Economic Geology, The University of Texas at Austin, Austin, TX. [2]Hildebrand Department of Petroleum and Geosystems Engineering, The University of Texas at Austin, Austin, TX [3] Earth and Environmental Sciences, Temple University, Philadelphia, PA

*Corresponding author: Owen A. Callahan (ocallahan@utexas.edu)

Key Points:

- Rock and fracture mechanical parameters of altered and damaged fault zone rocks differ significantly from those of the protolith.
- Silicification increases compressive strength, fracture toughness, and subcritical index relative to chlorite-calcite altered rocks.
- Sealing of >85-90% of microfractures by quartz and calcite is associated with strength recovery.

Abstract

Damaged and hydrothermally altered rocks are ubiquitous in fault zones, with the degree of damage and type and intensity of alteration varying in space and time. The impact of damage and alteration on hydromechanical properties of fault zones is difficult to assess without characterizing the associated changes to rock and fracture mechanical parameters. To evaluate the mechanical properties of fault rocks from different alteration regimes, we conducted 1) double-torsion load-relaxation tests to measure mode-I fracture toughness (K_{IC}) and subcritical fracture growth index (SCI), 2) uniaxial testing to measure unconfined compressive strength (UCS) and static elastic parameters, and 3) mineralogic and textural characterization of rock from four sites in the footwall of the Dixie Valley-Stillwater fault zone. Alteration at these sites includes: acid sulfate alteration and silicification associated with active fumaroles, intense silicification after calcite and chlorite alteration in an epithermal setting, quartz-kaolinite-carbonate alteration from an intermediate depth system, and a calcite-chlorite-hematite assemblage containing abundant unhealed damage. Silicification is associated with high K_{IC}, SCI, UCS, and increased brittleness, and in precipitation-dominated settings produces fault cores that are as strong or stronger than adjacent damage zone material. Calcite-chlorite-hematite assemblages containing abundant unsealed microfractures are approximately 4-5 times weaker than the granodiorite protolith. Mechanical properties are not predicted by mineralogical composition alone; a key control is the accumulation of damage and degree of healing. Measures of strength increase when mineral precipitation reduces microfracture porosity to <10-15% of total microfracture area. These results show that fault-proximal weakening or strengthening is influenced by hydrothermal setting.

1 Introduction

Fault-fracture networks contribute critically to fluid flow in low-porosity crystalline rock, impacting the distribution of heat, fluid, and minerals in the upper crust. Hydraulically

Post-print of
https://doi.org/10.1029/2018JB016708

conductive faults and fault segments are characterized by well-developed damage zones composed of opening-mode and sheared fractures (Brown & Bruhn, 1996; Caine et al., 1996; Sibson, 1996; Nelson et al., 1999; Davatzes & Aydin, 2003; Davatzes et al., 2003; Eichhubl et al., 2009; Anders et al., 2013). The occurrence of opening-mode fractures in and around fault zones, and the evolution of these flow systems from single fractures to complex interconnected networks by fracture reactivation, propagation, and coalescence provide a fundamental control on the permeability evolution of faults and fault-controlled hydrothermal and epithermal systems (Sornette, 1999; Davatzes et al., 2003; Davatzes et al., 2005; Blenkinsop, 2008).

Chemical controls on conduit evolution are well documented in field, experimental, and numerical studies, with dissolution, precipitation, and chemical alteration impacting the hydraulic properties of fault-facture networks (Summers et al., 1978; Moore et al., 1983; Berkowitz, 2002; Eichhubl et al., 2004, 2009). These effects are particularly pronounced in chemically reactive environments encountered in high temperature hydrothermal systems (Lowell et al., 1993), where dissolution, advection, and precipitation of different mineral species in response to thermal and chemical disequilibrium and water-rock reactions lead to the development of distinct alteration assemblages (Facca & Tonani, 1967; Henley & Ellis, 1983; Simmons et al., 2005; Tosdal et al., 2009; Sillitoe, 2010). Large regions of alteration are commonly associated with active hydrothermal systems (Browne, 1978) and around fossil conduits associated with magmatic and hydrothermal ore deposits (Henley & Ellis, 1983). However, some degree of alteration is common in most fault zones, where fracture-enhanced fluid flow and mechanical grain size reduction promote chemical reactions (Bruhn et al., 1994; Solum et al., 2010).

Mineralogical and textural changes associated with fault zone damage, fluid flow, and hydrothermal alteration result in hydromechanical properties that differ from those of relatively pristine samples commonly used in geomechanical laboratory tests. For example, Seront et al. (1998) showed a decrease in porosity and permeability of argillically altered fault core samples collected from the Dixie Valley-Stillwater fault zone, Nevada, with cemented damage zone rocks exhibiting a 7-115% increase in compressive strength. Wyering et al. (2014) and Siratovich et al. (2014) reported higher UCS in calcite and quartz ± propylitic altered volcanic rocks than in the same rocks dominated by quartz and clay alteration in the Taupo Volcanic Zone, New Zealand. Allen et al. (2017) showed damage, fluid-rock interaction, and mineralization near the principal slip zone of the Alpine Fault, New Zealand, resulted in reduced seismic velocity and permeability, and increased anisotropy of both properties, relative to intact country rock. Less work addresses the impact of damage and alteration on the fracture mechanical parameters fracture toughness (K_{IC}) and subcritical fracture growth index (SCI) (Atkinson, 1984; Kobayashi et al., 1986; Major et al., 2018), despite 1) the importance of fractures and fracture growth in fault systems and 2) distinct differences between naturally altered and damaged fault rocks and relatively pristine geomechanical materials.

For opening-mode (mode-I) fractures, the stress intensity at the fracture tip, K_I, may be written as a function of remote applied stress, σ_r, fracture length or height, a, and fracture geometry, Y (Brown & Strawley, 1966):

$$K_I = \sigma_r Y \sqrt{a} \qquad \text{Eq. 1}$$

Mechanical fracture propagation occurs when K_I reaches a critical threshold, known as fracture toughness (K_{IC}). K_{IC} is more influential during early fracture growth when fracture length, a, is small and K_I is proportionally lower (Engelder et al., 1993). Cyclic loading and chemical corrosion at the fracture tip can lead to fracture growth below the critical stress intensity threshold, referred to as subcritical fracture growth. Subcritical fracture growth is quantified by the SCI parameter, which describes the relationship between fracture propagation velocity and stress intensity for fracture propagation below K_{IC} in the empirically derived equation (Pletka et al., 1979):

$$V = V^* \left(\frac{K_I}{K_0}\right)^{SCI} \quad \text{Eq. 2}$$

where V is velocity, V^* is a constant, and K_0 is a normalization factor. Subcritical fracture growth has been invoked to explain long-term strength of the crust (Anderson & Grew, 1977; Rudnicki, 1980; Brantut et al., 2013), and differences in SCI may influence fracture spatial arrangements (Olson, 1993, 2004). Together, K_{IC} and SCI characterize key fracture mechanical properties in a deforming rock volume.

Post-print of
https://doi.org/10.1029/2018JB016708

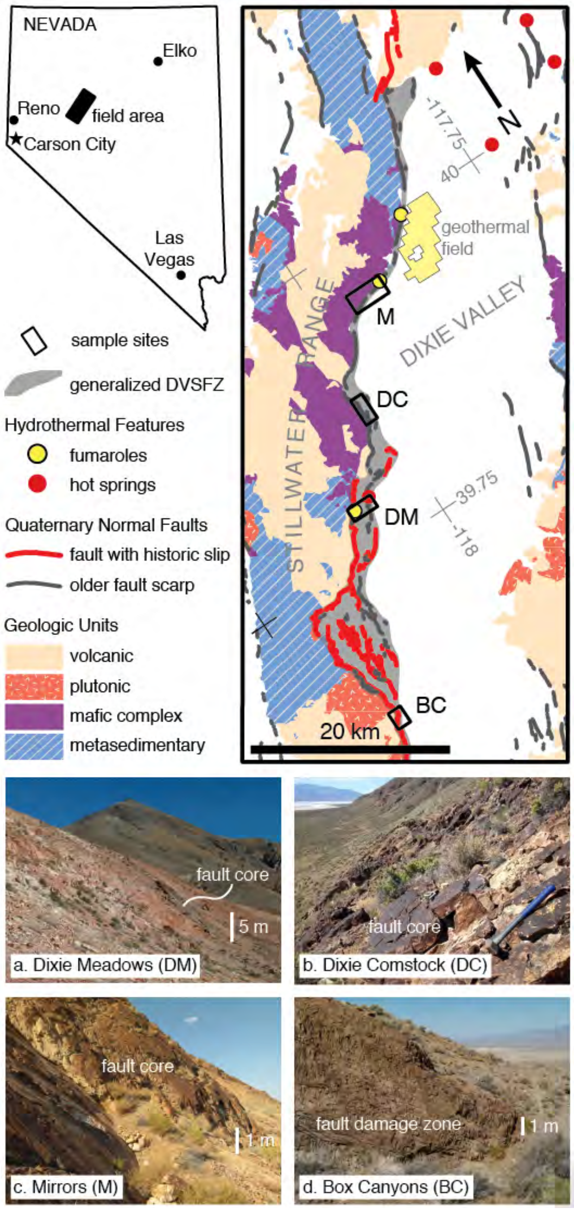

Figure 1. Field sites in the Dixie Valley – Stillwater fault zone (DVSFZ), Nevada, include Dixie Meadows fumaroles (DM), Dixie Comstock epithermal gold deposit (DC), the Mirrors (M), and the Box Canyons (BC). Parts a-d show representative field photographs from each site. Active hydrothermal circulation within the Dixie Valley – Stillwater Fault zone manifests as hot springs and fumaroles, and is utilized for electricity generation in the Dixie Valley geothermal production area (Berry et al., 1980; NREL, 2016). Quaternary faults after USGS and NBMG (2010). Geology modified from Crafford (2007).

Here we present experimental measurements of K_{IC} and SCI from double-torsion load-relaxation (DT-LR) fracture mechanics tests of samples of hydrothermally altered and damaged rocks collected from four sites in the Dixie Valley – Stillwater fault zone, Nevada (Figure 1, Table 1). Sample sites represent a variety of hydrothermal settings, including: 1) shallow acid sulfate alteration at Dixie Meadows fumaroles, 2) epithermal silicification after chlorite-calcite alteration at Dixie Comstock, 3) quartz-kaolinite-carbonate alteration and cementation in the "Mirrors" normal fault exposure, and 4) chlorite-calcite-hematite dominated assemblages at the Box Canyons. Alteration and deformation histories at these sites record exhumation from different temperatures, depths, and hydrothermal conditions (Figure 2) constrained by mineral assemblages, mineral textures, fluid inclusion homogenization temperatures, and geologic relationships, and illustrate the relative impact of damage-dominated versus precipitation-dominated settings on fracture mechanical behavior. We demonstrate that hydrothermal alteration, previously recognized as an important factor influencing rock mechanical properties, also impacts the fracture mechanical properties influencing initiation, growth, and coalescence in fault-fracture networks.

***Table 1**. Sample Naming and Descriptions*

Site[a]	ID[b]	Field name	IGSN[c]	Material and alteration
DM	1	052615-3A	IECAL003L	tuff; minor argillic
	2	052615-3B	IECAL003M	fault breccia; cemented
DC	3	083114-2A	IECAL0028	gabbroic; albite, minor chlorite
	4	052815-3B	IECAL001I	gabbroic; chlorite
	5	052815-3A	IECAL001H	gabbroic; calcite, chlorite
	6	061114-4B	IECAL001W	fault breccia; silicified
	7	052815-2	IECAL001G	fault breccia; silicified
M	8	030914-1	IECAL003S	mafic plutonic; quartz, kaolin
	9	052715-7A	IECAL003T	fault breccia; cemented
BC	10	052615-1A	IECAL0004	granodiorite
	11	052615-1B	IECAL0005	granite
	12	071813-3	IECAL000F	granite; damaged zone
	13	071813-2	IECAL000E	damage zone; chlorite, calcite
	14	052615-2	IECAL0006	damage zone; chlorite, calcite

[a] DM = Dixie Meadows. DC = Dixie Comstock. M = Mirrors fault zone. BC = Box Canyons. [b] Sample ID numbers used in the text, tables, and figures. [c] Searchable International Geo Sample Number (http://www.geosamples.org).

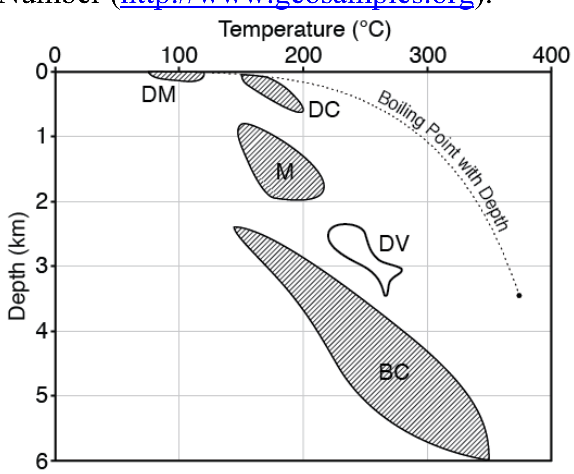

Figure 2. Temperature-depth conditions during development of dominant alteration assemblages at each site. DM = Dixie Meadows, DC = Dixie Comstock, M = Mirrors, BC = Box Canyons. Temperature-depth constraints for each sample site are discussed in the text. Average temperature in the producing Dixie Valley geothermal reservoir (DV) is ~248 °C at 2.5-3 km, with recorded temperatures as high as 285 °C (Blackwell et al., 2007). Boiling point with depth for pure water from Haas (1971).

2 Geologic Setting

The Dixie Valley – Stillwater fault zone is a north to northeast striking, east dipping basin-bounding normal fault system in northwest Nevada, USA (Figure 1). The Stillwater Range is composed of Triassic phyllite, Jurassic mafic igneous and volcanic rocks of the Humboldt Igneous Complex and associated sedimentary facies, small Cretaceous granitic plutons, and Oligocene plutonic and volcaniclastic sequences, and is capped by mid-Miocene basalt (Page, 1965; Speed & Jones, 1969; Speed, 1976; Dilek & Moores, 1995; John, 1995; Kistler & Speed, 2000). The basin hosts a series of buried, nested grabens with >1.8 km of Quaternary lacustrine and alluvial fan deposits (Okaya & Thompson, 1985; Bell & Katzer, 1990). Post 8 Ma dip-slip displacement in northern Dixie Valley is between 2.2-2.9 km (Okaya & Thompson, 1985) and post-Oligocene slip in southern Dixie Valley may exceed 6 km (Thompson et al., 1967; Parry & Bruhn, 1990).

The region has attracted attention in part due to its location at the northern end of the Central Nevada Seismic Belt (Wallace, 1984; Wallace and Whitney, 1984; Bell et al., 2004). Historic seismicity in the Dixie Valley region includes: 1903 Wonder (~M6.5?), 1915 Pleasant Valley (Ms 7.6-7.8), the 1954 Rainbow mountain sequence (Ms 6.3-7.0), and the 1954 Fairview Peak – Dixie Valley sequence (M 7.2 to 6.8) (Slemmons, 1957; Wallace, 1984; Bell and Katzer, 1990; Caskey et al., 1996; Caskey et al., 2004; Bell et al., 2004). Fault scarps from the 1954 Dixie Valley earthquake parallel the Stillwater Range through the southern portion of the field area, with older Quaternary fault scarps located throughout the Dixie Valley – Stillwater fault zone (Figure 1).

The Dixie Valley geothermal field in northern Dixie Valley nets ~56 MWe from ~248 °C fluids hosted in faulted and fractured Miocene basalt and Jurassic and Cretaceous plutons at ~2.5-3 km depth (Benoit, 1992, 2015; Blackwell et al., 2000, 2007). Smaller producing geothermal fields and prospective resources occur north and south of the main installation. Surface hydrothermal manifestations include fumaroles and hot springs, and fossil sinter and travertine deposits (Lutz et al., 2002). Older exhumed hydrothermal alteration assemblages include regional sodic and calcic metasomatism of Jurassic mafic rocks (Dilek & Moores, 1995; Johnson & Barton, 2000), syn-magmatic potassic and sericite alteration of Oligocene granitic rocks (Parry et al., 1991; Bruhn et al., 1994; John, 1995), and retrograde, fault-related sericite, chlorite-carbonate-hematite, quartz-kaolinite, smectite, zeolite, and silicic assemblages in local segments of the fault system (Power & Tullis, 1989; Parry et al., 1991; Vikre, 1993; Bruhn et al., 1994; Caine et al., 2010).

3 Methods

3.1 Mineralogical and Textural Characterization

We evaluated bulk mineralogy of damaged and altered rocks with X-ray diffractometry (XRD) using a Bruker D8 Advanced X-ray Diffractometer with LynxEye detector (Table 2). Samples were prepared as randomly oriented spray-dried powders (Hillier, 1999) and scanned at ~0.01° increments from 4-66° 2-theta for 1.5-2 hrs. Initial analysis of XRD spectra was conducted with EVA software, followed by Rietveld analysis using TOPAS 4.2 software. Methods and spectra are included in the archived data (Callahan, 2019).

Alteration products and reactants were further described with thin section petrography. Host rock porosity, microfracture porosity, and microfracture porosity occluded by mineral cements were measured using point counting of blue-epoxy impregnated thin sections at 120X magnification and approximately 400 points per sample (Table 3). Total microfracture area was calculated from the sum of points encountering microfracture porosity or cement. Thin sections were oriented approximately perpendicular to the dominant structural fabric.

Table 2. *Bulk Mineralogy from X-ray Diffraction of Spray Dried Powders*

Site	ID	Setting[a]	Cor spike[b] (wt%)	Cor[c] (wt%)	Normalized wt%												
					quartz	other feldspar	albite	amphibole	pyroxene	biotite	carbonate[d]	epidote	chlorite	muscovite	kaolin	other clay	oxides, sulfides
DM	1	dmg	10.14	10	50	38	-[e]	-	-	-	-	-	-	-	6	7	<1
	2	core	9.98	10	40	7	-	-	-	-	54	-	-	-	-	-	-
DC	3	dmg	10.00	9	10	30	46	-	-	-	<1	2	8	2	-	-	2
	4	dmg	9.98	9	2	33	26	-	-	-	1	1	32	4	-	-	-
	5	dmg	10.16	9	1	36	21	-	-	-	19	-	22	-	-	-	1
	6	core	10.00	7	91	5	<1	-	-	-	-	-	4	-	-	-	<1
	7	core	10.00	6	97	-	<1	-	-	-	<1	-	3	-	-	-	<1
M	8	dmg	10.00	10	49	-	-	-	-	-	8	-	-	3	40	-	<1
	9	core	10.00	10	60	-	-	-	-	-	10	-	-	2	28	-	<1
BC	10	proto	9.98	10	23	44	18	7	2	4	-	-	-	1	-	-	-
	11	proto	10.00	10	33	46	20	-	-	<1	-	-	-	1	-	-	<1
	12	dmg	10.00	10	24	51	14	2	6	1	-	-	-	2	-	-	<1
	13	dmg	10.00	10	29	40	14	-	-	-	7	1	9	-	-	-	-
	14	dmg	10.00	10	19	46	21	-	-	-	2	<1	6	5	-	-	1

[a] Fault setting, proto = protolith, dmg = damage zone, core = fault core. [b] Corundum spike added to milled samples. [c] Corundum in final Rietveld solutions [d] Predominantly calcite, except samples 8 and 9 which also contain Fe- and Mg- rich carbonates. [e] '-' not included in final Rietveld solution.

Post-print of
https://doi.org/10.1029/2018JB016708

***Table 3**. Sample Properties from Point Counting*

Site	ID	Setting	Total porosity (%)			Fracture porosity (%)			Fracture cement (%)			Total fractured area (%)			Sealing (%)	n
				+	-		+	-		+	-		+	-		
DM	**1**	dmg	7.1	2.4	1.9	0.0	0.7	0.0	0.7	1.1	0.5	0.7	1.1	0.5	100	434
	2	core	0.3	1.0	0.3	0.0	0.8	0.0	2.7	1.8	1.2	2.7	1.8	1.2	100	371
DC	**3**	dmg	0.7	1.2	0.5	0.7	1.2	0.5	5.3	2.3	1.8	6.0	2.4	1.9	89	383
	4	dmg	1.8	1.4	0.9	1.1	1.2	0.7	0.7	1.1	0.5	1.8	1.4	0.9	38	418
	5	dmg	0.7	1.1	0.5	0.0	0.7	0.0	3.6	1.9	1.4	3.6	1.9	1.4	100	451
	6	core	0.5	1.1	0.4	0.2	0.9	0.2	6.7	2.4	1.9	6.9	2.4	2.0	96	404
	7	core	1.6	1.5	0.9	0.8	1.3	0.6	11.8	3.1	2.6	12.6	3.1	2.7	93	381
M	**8**	dmg	0.6	1.0	0.5	0.4	0.8	0.3	2.8	1.5	1.1	3.2	1.6	1.2	88	504
	9	core	0.3	0.6	0.2	0.0	0.5	0.0	5.0	1.6	1.3	5.0	1.6	1.3	100	659
BC	**10**	proto	0.0	0.7	0.0	0.0	0.7	0.0	0.2	0.9	0.2	0.2	0.9	0.2	100	410
	11	proto	0.5	1.0	0.4	0.3	0.9	0.3	3.0	1.7	1.2	3.3	1.8	1.3	92	428
	12	dmg	2.0	1.6	1.0	1.7	1.6	0.9	3.8	2.0	1.5	5.5	2.3	1.8	68	382
	13	dmg	5.6	2.2	1.7	5.1	2.1	1.6	14.3	3.1	2.7	19.4	3.5	3.1	74	418
	14	dmg	2.5	1.7	1.1	2.5	1.7	1.1	20.8	3.6	3.2	23.3	3.7	3.4	89	412

3.2 Unconfined Compressive Strength and Static Elastic Characterization

We measured static elastic properties and unconfined compressive strength (UCS) with uniaxial compressive strength tests using a GCTS rock mechanics system (Table 4). Plug orientations were vertical (V), parallel to strike (H), down dip (D), or mutually perpendicular to strike and dip (P) of local range front faults. Plug diameter was 25.4 mm and average plug length was approximately 53.0 mm. Loading was conducted at a preprogrammed axial strain rate of 0.055%/minute (~0.5 μm s^{-1}). UCS is reported from peak, area-corrected load. Young's modulus and Poisson's ratio were calculated from the middle portion of the loading curve where the relationship between stress and strain was approximately linear. Complete load curves are included in the archived data (Callahan, 2019).

***Table 4.** Unconfined Compressive Strength and Static Elastic Properties*

Site	ID	Setting	UCS (MPa)		E (GPa)		ν		G (GPa)		n
			mean	± std dev	mean	± std dev	mean	± std dev	mean	± std dev	
DM	**1**	dmg	62.4	10.3	15.1	0.8	0.10	0.06	6.9	0.0	2
	2	core	68.1	11.3	27.2	7.0	0.16	0.05	11.6	2.7	4
DC	**3**	dmg	-	-	-	-	-	-	-	-	-
	4	dmg	50.7	-	22.8	-	0.20	-	9.5	-	1
	5	dmg	148.0	-	48.2	-	0.22	-	19.7	-	1
	6	core	187.8	-	51.1	-	0.13	-	22.6	-	1
	7	core	286.5	12.7	62.8	1.6	0.11	0.02	28.3	0.3	2
M	**8**	dmg	67.1	-	27.0	-	0.38	-	9.8	-	1
	9	core	109.0	8.9	38.9	3.0	0.13	0.03	17.3	1.5	5
BC	**10**	proto	256.2	14.4	59.4	2.2	0.29	0.03	23.1	0.3	2

11	proto	99.8	20.8	40.0	5.6	0.24	0.04	16.1	1.7	2
12	dmg	-	-	-	-	-	-	-	-	-
13	dmg	-	-	-	-	-	-	-	-	-
14	dmg	51.1	5.5	17.6	2.2	0.25	0.10	7.0	0.4	3

3.3 Double-Torsion Load-Relaxation Fracture Mechanics Testing

We used double-torsion load-relaxation (DT-LR) tests to measure K_{IC} and SCI using multiple specimens of altered rocks. DT-LR tests were conducted by repeatedly propagating a fracture down the axis of a specimen prepared as a thin rectangular wafer (Figure 3a). All specimens were cut from the same blocks of material used for petrographic, mineralogic, and mechanical characterization. Specimens were cut so the propagation directions of induced fractures were typically vertical and/or parallel to the local structural grain, although this was limited by poor material quality in some samples. Orientation information for each wafer is included in the archived data (Callahan, 2019). Detailed descriptions of the testing apparatus, method, and data reduction procedure used here can be found in Chen et al. (2017), and are summarized below.

The DT testing apparatus consists of a base plate, specimen supports, a loading ram with internal force sensor, and a linear variable displacement transducer to record displacement (Figure 3b). K_I at the fracture tip was calculated using the equation (Williams & Evans, 1973):

$$K_I = PW_m\sqrt{\frac{3(1+\nu)}{\varphi W t_n t^3}} \qquad \text{Eq. 3}$$

where P is load supported by a pre-fractured specimen, W_m is the moment arm of the DT apparatus, ν is Poisson's ratio, W is specimen width, t is specimen thickness, and t_n is the reduced thickness along an axial groove created by pulling the specimen across a recessed diamond saw prior to testing (Figure 3c). If insufficient sample material existed for UCS tests, ν was estimated from similarly altered and damaged samples. The geometric correction factor, ψ, is based on individual specimen geometry (Fuller, 1979):

$$\psi = 1 - 0.6302\frac{2t}{W} + 1.2\frac{2t}{W}e^{\left(\frac{-\pi W}{2t}\right)} \qquad \text{Eq. 4}$$

We tested specimens with thickness (t), width (W), and length (L) dimensions of approximately 1.8 mm x 30 mm x 75 mm, respectively, meeting dimensional requirements of ~24t<2W<L (Nara & Kaneko, 2005). Absolute specimen dimensions were similar to those used by Atkinson (1979b), Sano et al. (1992), and Chen et al. (2017) and were limited in part by sample size and load cell capacity. Pre-fractures were induced using the DT apparatus at low displacement rates (<1 μm/s) until a distinct load drop was observed, indicating the formation of an edge crack.

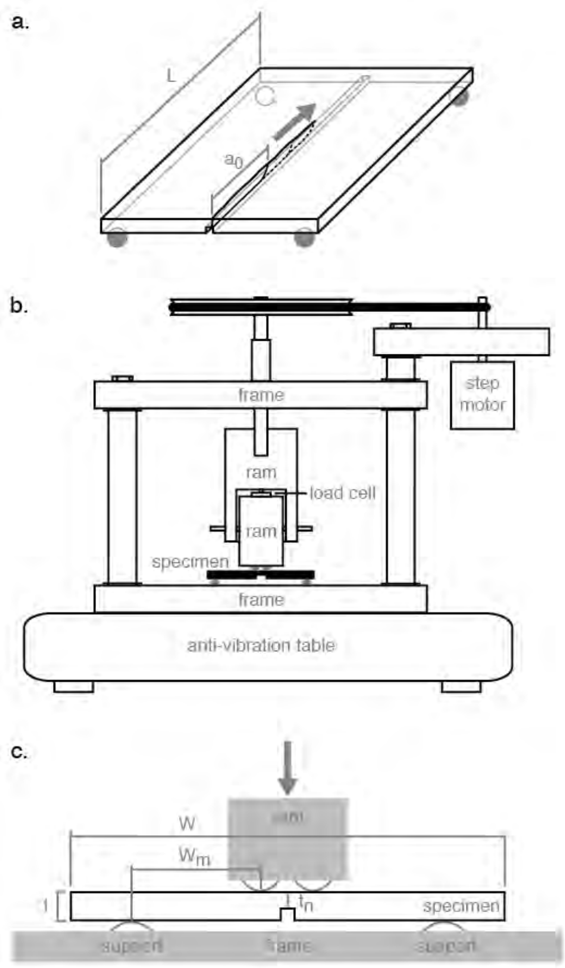

Figure 3. Double-torsion test schematic, apparatus, and specimen geometry. a) Oblique view of specimen showing induced pre-fracture length (a_0) and subsequent fracture growth increments during load-decay tests. Arrow indicates direction of fracture propagation. b) Double-torsion apparatus. c) Cross-section of double-torsion specimen, with load and support points (semicircles) and dimensions: W = width, W_m = moment arm, t = thickness, t_n = reduced thickness.

DT tests for fracture toughness were conducted on pre-fractured specimens at fast displacement rates (180-220 µm/s) to total failure (Figure 4a). DT-LR tests for SCI were conducted by loading pre-fractured specimens at low displacement rates (1-2 µm/s) until fracture propagation was indicated by a rapid drop in supported load. Displacement was stopped, and the load allowed to decay for 5-10 minutes. Ideal DT-LR test patterns included a high pre-fracture load, a subsequent plateau region of lower peak loads and load-decay curves that were used to calculate SCI, and a final load drop upon complete specimen failure (Figure 4b). A separate estimate of fracture toughness (K_{IC}*) based on the stress intensity from peak loads in the plateau region during slow displacement tests was evaluated as a proxy for K_{IC}. Load and displacement were recorded at 14 Hz for DT tests and 5 Hz for DT-LR tests. All tests were conducted under ambient conditions at 23-24°C. Relative humidity was not measured for all tests, but commonly ranged between 58-75% and could have contributed small variations to test results (Nara et al., 2012).

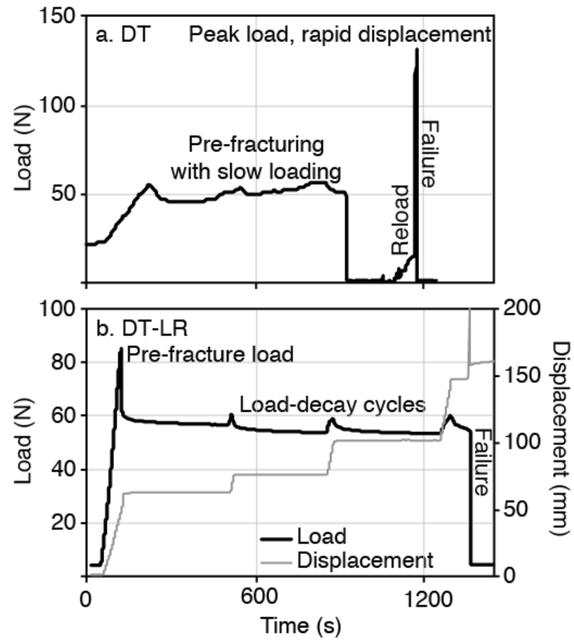

Figure 4. Load and displacement patterns from DT tests. a) DT test pattern during rapid loading to failure used to derive K_{IC}. b) Slow loading, DT-LR tests used to derive SCI and K_{IC}*. SCI is derived from load-decay cycles at constant displacement. K_{IC}* is derived from local load maxima sustained at the start of each load-decay cycle.

Fracture propagation velocity was calculated from the load relaxation curve (Evans, 1972):

$$V = -\phi\left(\frac{a_0 P_i}{P^2}\right)\frac{dP}{dT} \qquad \text{Eq. 5}$$

where a_0 is initial fracture length, and P_i is load at the start of each load-decay cycle. The correction factor for fracture front geometry, ϕ, was assumed to be 0.2 (Williams & Evans, 1973; Atkinson, 1979a; Chen et al., 2017). Because pre-fracture lengths were difficult to observe in these materials, we followed Chen et al. (2017) and use a_0 of 12.7 mm, with later cycles using $a_n = a_0 + n*12.7$ mm, a nominal value that accounts for the average number of fracture growth increments and specimen length. Variation of a_0 has limited impact on calculated fracture front velocity (Chen et al., 2017). SCI was calculated from K-V curves using an in-house LabView script for smoothing and fitting following derivations described in Holder et al. (2001). Individual specimen dimensions, peak loads, K_{IC}, K_{IC}*, derived SCI, and load-decay curves are included in the archived data (Callahan, 2019).

4 Sample Sites and Materials

4.1 Acid Sulfate Alteration and Silicification at Dixie Meadows Fumaroles

The Dixie Meadows fumaroles site is located near the northern terminus of the 1954 Dixie Valley fault rupture and west of Dixie Meadows Hot Springs (Figure 1). At this site, fumarole-related alteration in Oligocene tuff is exposed in the footwall of the Dixie Valley – Stillwater fault zone. Alteration products here include native sulfur, sulfate minerals, kaolin group minerals, montmorillonite, calcite, and quartz (Kennedy-Bowdoin et al., 2004; Lamb et al., 2011; Schwering, 2013), a suite of minerals reflecting shallow acid sulfate alteration related to ongoing fumarole activity and boiling or near boiling conditions in the shallow subsurface (Figure 2).

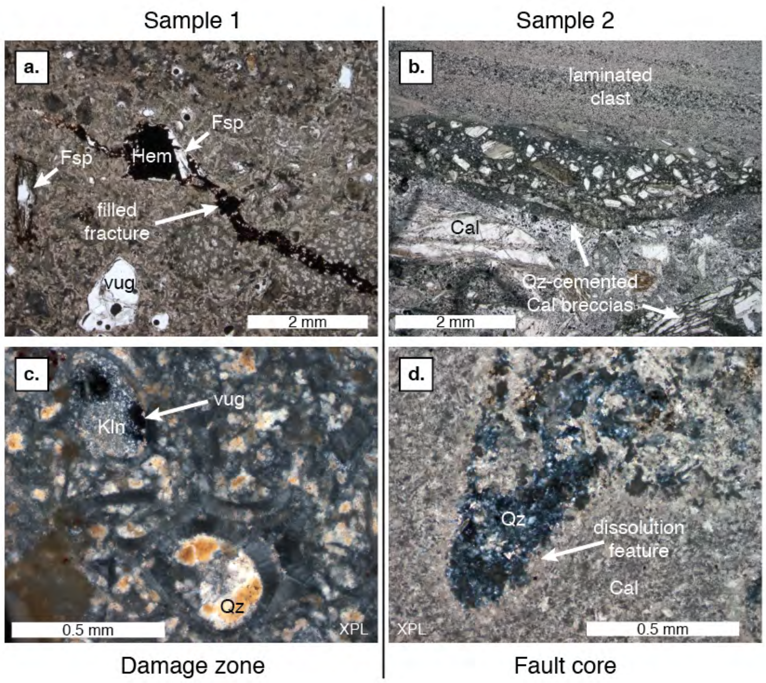

Figure 5. Photomicrographs of Dixie Meadows samples. Sample 1 (a, b) contains quartz (Qz), hematite (Hem), kaolinite (Kln) alteration of Oligocene tuff in the damage zone at Dixie Meadows. Sample 2 (c, d) is a microquartz-cemented fault breccia with abundant calcite clasts (Cal). Abbreviations after Whitney and Evans (2010).

We tested multiple plugs and DT specimens from two samples from Dixie Meadows Fumaroles: a moderately altered tuff (sample 1), and a portion of exhumed fault core composed of weakly silicified bladed calcite and microquartz (sample 2) (Figure 5, Table 2). Sample 1 is a pale, non-welded, devitrified tuff, with partially dissolved feldspar phenocrysts. The dominant mineral species are quartz and feldspar, with lesser kaolinite and undifferentiated clay. Vugs in pumice are commonly filled with kaolinite, whereas vugs in partially dissolved feldspar grains contain small euhedral quartz crystals. Hematite occurs as disseminated grains and as fracture fill. Pores are typically smaller than 0.5 mm, with some secondary pores in dissolved grains exceeding 2 mm. Total porosity is ~7.1%, and total microfracture area is low (~0.7%) (Table 3). Sample 2 is coarse-grained fault breccia, mineralogically and texturally dominated by multiple generations of quartz and calcite, with minor hematite and sericite. Calcite occurs as bladed laths and as disseminated, fine-grained, intergrowths with microquartz. Microquartz occurs as clasts and as cement between clasts. Clast sizes range from 1 cm to <1 mm. Total porosity and total microfracture area are low (0.3% and 2.7%, respectively).

4.2 Na-Ca Alteration and Silicification at Dixie Comstock Epithermal Gold Deposit

The Dixie Comstock epithermal gold deposit is located along a north-striking portion of the Dixie Valley – Stillwater fault zone (Figure 1). Several temporally distinct episodes of alteration are preserved in the Dixie Comstock area. Early and widespread sodic and calcic alteration of the Jurassic Humboldt Igneous Complex (Dilek & Moores, 1995; Johnson & Barton, 2000) is overprinted by aureoles of quartz, albite, sericite, kaolinite, and iron oxide around apophyses of Cretaceous granite (Vikre, 1993). Alteration in the mine area is dominated by silicification of the range front fault, with portions of the silicified fault core exceeding 2 m in thickness and approaching 100% quartz. Silicification overprints and entrains earlier assemblages. Intense silicification extends ~300 m north and south of the mine workings, with quartz veins in the footwall and minor silicification of fault breccia extending 1.5 km along strike and at least several hundred meters down dip. Bladed calcite (this study) and liquid- and vapor-rich inclusions (Vikre, 1993) indicate boiling conditions existed in shallow parts of the system, and fluid inclusion microthermometry indicate temperatures between 160-180 °C (Vikre, 1993). Boiling near 170 °C suggests exhumation from as shallow as 76 m (Haas, 1971) (Figure 2).

Dixie Comstock samples were obtained from a distal portion of the footwall (sample 3), from the footwall behind the main mineralized deposit (samples 4 and 5), and from the silicified fault core (samples 6 and 7) (Figure 6). Alteration reactions are dominated by selective replacement of feldspars and mafic minerals with chlorite, calcite, and sericite and intense silicification (Table 2). Sample 3 is a medium-grained gabbro, dominated by plagioclase and altered mafic minerals. Alteration minerals include albite, chlorite, and minor quartz, epidote, sericite, sulfides, oxides, and trace calcite. Plagioclase is partially albitized, and exhibits minor chloritization and sericitization. Plagioclase laths are broken, but intragrain fractures have no observable porosity. Total porosity is low (~0.7%) and total microfracture area is intermediate (~6%). Samples 4 and 5 retain primary textures, but plagioclase and mafic minerals are increasingly replaced by chlorite in sample 4 and by calcite in sample 5. Plagioclase laths are cloudy. Calcite occurs as replacement and as thin cement lining fractures. Cataclastic zones contain crushed plagioclase and calcite with hematite and pyrite. Sample 4 has low total microfracture area (1.8%) and intermediate porosity (1.8%), whereas Sample 5 has higher total microfracture area (3.6%) and lower porosity (0.7%) (Table 3). Samples 6 and 7 were collected from different locations within the silicified fault core and reflect textural, mineralogical, and mechanical variations observed in this material. These samples are dominated by fine-grained, intergrown, microquartz with minor chlorite, feldspar, and plagioclase, and trace sericite, calcite, and sulfides and oxides. Both samples contain evidence of multiple generations of brecciation and quartz cementation in the form of broken and rounded clasts of earlier microquartz breccia. Total microfracture area in Sample 6 is intermediate (6.9%) and porosity is low (0.5%). Total microfracture area in Sample 7 is high (12.6%), but intense silicification has reduced porosity to 1.6%. In both samples, porosity is restricted to quartz lined and nearly occluded vugs and partially quartz- or calcite-cemented fractures.

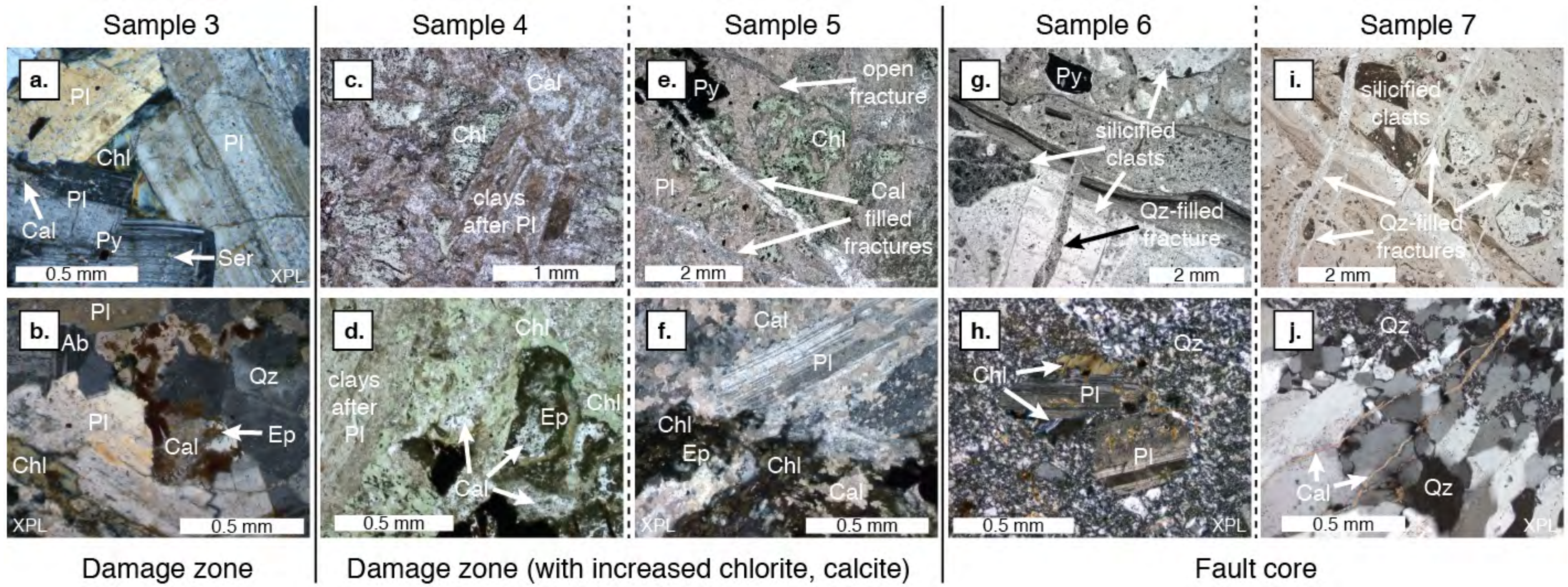

Figure 6. Photomicrographs of Dixie Comstock samples (3-7). Dixie Comstock samples show progressive alteration from background propylitic and Na-Ca altered gabbroic rocks through increased calcite-chlorite alteration and late silicification. Sample 3 (a, b) with chlorite (Chl), calcite (Cal), and epidote (Ep) after mafic minerals, sericite (Ser) and albite (Ab) in Ca-rich plagioclase (Pl), and secondary quartz from a distal portion of the damage zone. Samples 4 (c, d) and 5 (e, f) record increasing chloritization and calcification of plagioclase and mafic minerals and calcite-filled fractures near the mineral deposit. Fault core samples 6 and 7 (g-j) contain massive silicification, abundant quartz-filled fractures, and relict altered grains.

4.3 Quartz-Kaolinite-Carbonate Alteration at the "Mirrors" Fault Zone Exposure

The Mirrors site is located along a northeast-striking section of the Dixie Valley – Stillwater fault zone southwest of the producing geothermal field (Figure 1). The protoliths at the Mirrors are intrusive and extrusive components of the Jurassic Humboldt Igneous Complex (Page, 1965; Speed, 1976; Dilek & Moores, 1995). Alteration includes regional sodic, calcic, and chlorite alteration, with later kaolinite, carbonate, and quartz after mafic minerals and feldspars in well-developed fault damage zone and core (Lutz & Moore, 1996; Caine et al., 2010). Physical conditions during the dominate phase of alteration are constrained by post-Miocene exhumation of <2 km (Power & Tullis, 1989, 1992) and the occurrence of quartz with kaolinite indicating temperatures <270 °C (Figure 2). Ferroan dolomite, chalcedony, goethite, and barite (Lutz & Moore, 1996) and chalcedony with kaolinite (this study) indicate that at least some alteration occurred at temperatures <180 °C.

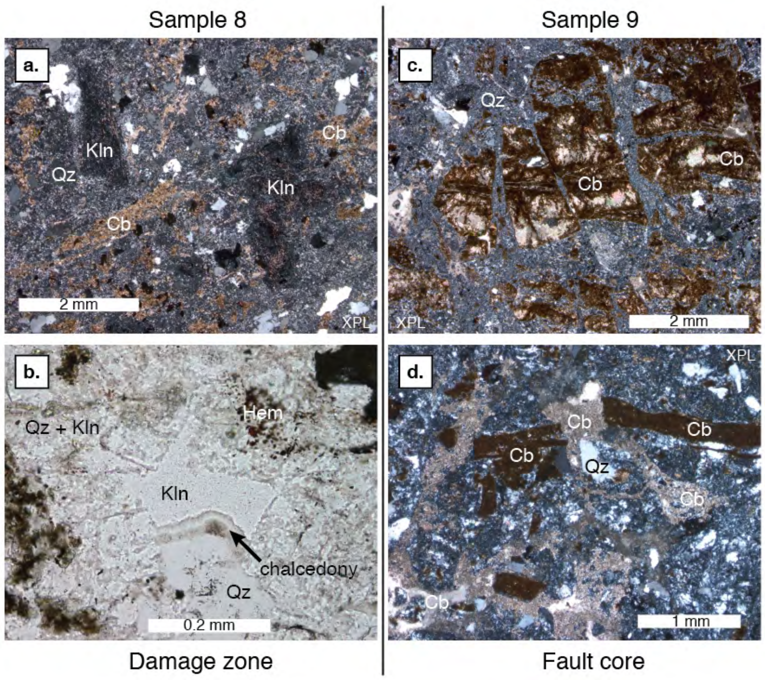

Figure 7. Photomicrographs of Mirrors samples (8 and 9). Sample 8 (a, b) includes replacement of feldspars by kaolinite (Kln), amphiboles by ankerite and calcite (Cb), hematite (Hem) and abundant quartz cement (Qz) in the fault damage zone. The occurrence of kaolinite with chalcedony indicates alteration continued <180 °C. Sample 9 (c, d) records multiple cycles of deformation and cementation by calcite, ankerite, and quartz in the fault core.

Samples from the Mirrors include altered and moderately silicified fault damage zone (Sample 8) and fault core material (Sample 9) (Figure 7, Table 2). Sample 8 is an argillic-silicic altered fine to medium grained mafic plutonic rock. Mineralogy is dominated by quartz and kaolinite, with lesser carbonate (calcite, ankerite), sericite, and trace hematite. Primary magmatic textures are cryptic, with kaolinite replacing feldspars, calcite replacing amphibole, and degraded pyroxene. Quartz is dominantly fine grained, intergrown microquartz, with rare chalcedony-lined, kaolinite-filled pockets. Carbonate occurs as small (<50 μm), disseminated grains, as fill in thin, discontinuous fractures, and replacing amphibole grains <2 mm long. Sample 9 was obtained from the cemented fault core. Sample texture is heterogenous at the thin section scale. Cement is dominantly fine grained, interlocking microquartz, with angular to sub-angular clasts <2 cm long of broken calcite and ankerite veins. Macroscopic textures indicate repeated brecciation, alteration, and cementation during exhumation, with little primary texture preserved. Kaolinite, sericite, and calcite occur in the matrix, with some sericite and carbonate replacing clasts. Samples 8 and 9 both contain intermediate total microfracture area (3.2 and 5.0%, respectively), and low total porosity (0.6 and 0.3%), similar to porosity between 0.3-0.4% previously measured in Mirrors fault core samples (Seront et al., 1998).

4.4 Chlorite-Calcite-Hematite Alteration and Damage at the "Box Canyons"

The Box Canyons site is located along a portion of the Dixie Valley – Stillwater fault zone that ruptured in the 1954 Fairview Peak – Dixie Valley earthquake sequence (Figure 1). Host lithology is Oligocene-Miocene granite and granodiorite (John, 1995). Fault-proximal alteration records progressive exhumation, with early, deep, potassium feldspar-biotite to chlorite-calcite-hematite ±epidote alteration, sericite-quartz-kaolinite-smectite and zeolite alteration (Parry et al., 1991; Bruhn et al., 1994). Oligocene-Miocene K-Ar ages from sericite are coeval with magmatism (Parry et al., 1991). Alteration occurred across a range of depth and temperature conditions (Figure 2). Mineral equilibrium and fluid inclusion studies indicate potassic alteration occurred at <6 km and 300-350 °C (Parry & Bruhn, 1990; Parry et al., 1991). Epidote, chlorite, calcite assemblages record alteration >240 °C. Parry et al. (1991) reported homogenization temperatures in fluid inclusions in microfractures in quartz as low as 180-190 °C and stilbite in outcrop, suggesting alteration continued <140 °C and <2.5 km, although we did not observe zeolite locally.

Box Canyon samples (10-14) record increasing alteration and damage of granite and granodiorite (Figure 8, Table 2). Background samples include two plutonic phases: a less altered granodiorite (Sample 10) and a more altered granite (Sample 11). Quartz grains in sample 10 contain minor deformation. Plagioclase laths up to 1.5 mm in length contain small, uneven fractures, but no rotation and only minor sericitization. Biotite and amphibole are relatively pristine. All crystals are intergrown, with little interstitial space, no observed porosity, and low total microfracture area (0.2%). Feldspars in Sample 11 contain patches of albite, and cloudy, vacuolized cores. Damage includes transgranular fractures with minor, early hydrothermal biotite. Total microfracture area is intermediate (3.3%) with low porosity (0.5%). Sample 12 was collected near the range front fault, but away from the chlorite-calcite-hematite altered area. Hydrothermal biotite replaces mafic minerals and occurs as fracture fill in orthoclase. Feldspars and some plagioclase laths contain cloudy, vacuolized cores, large sericite grains, and increased albitization. Porosity (2%) is comparable to 1.2% previously reported for Box Canyon damage zone samples (Seront et al., 1998), and occurs in microfractures and in partially dissolved feldspars. Total microfracture area is intermediate (5.5%). Samples 13 and 14 were both collected from the most altered area in the Box Canyons site, the “ultra damaged carapace” of Seront et al. (1998), and contain among the highest microstructural heterogeneity at the thin section and specimen scale. Alteration minerals include carbonate and chlorite, with lesser sericite, epidote, and sulfides and oxides. Damage includes multiple cross-cutting cataclastic bands, broken grains, and thin, partially calcite- and hematite-filled fractures (Figure 8). Total microfracture area is high (19.4-23.3%). Porosity (2.5-5.6%) occurs in late, partially calcite-filled fractures, and at the edges of cataclastic bands.

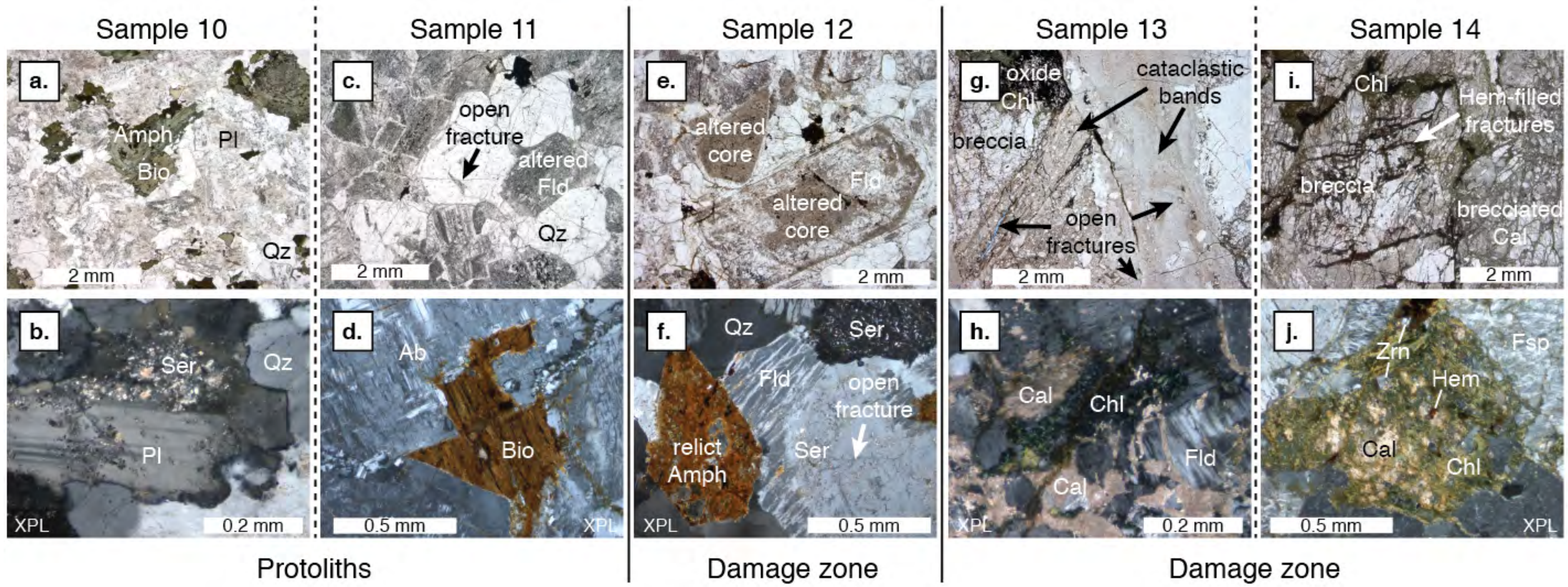

Figure 8. Photomicrographs from Box Canyon samples (10-14). Alteration in background granodiorite (Sample 10; a, b) and granite (Sample 11; c, d) includes minor sericitization (Ser) of feldspar (Fld) and albitization (Ab) of plagioclase (Pl). Damage zone Sample 12 (e, f) contains relict amphibole (Amph), sericite (Ser), and increased microfracture porosity. Samples 13 and 14 are obtained from the most altered and damaged area at the Box Canyons and include extensive replacement of plagioclase with calcite (Cal) and chlorite (Chl), partially calcite- and hematite- (Hem) cemented fractures, open fractures, and cataclastic (g-j). Damage increases from isolated open fracture to cataclastic bands (g) and intense brecciation or fragmentation of grains and veins (i).

5 Experimental Results and Analysis

5.1 UCS and Static Elastic Properties

We conducted UCS tests on 24 plugs from 11 samples of crystalline rock with varying types and degrees of alteration and damage (Table 4, Figure 9). The number of successful repeat tests was limited in some samples by the amount and quality of sample material. When multiple orientations were tested, strength and elastic measurements from plugs with different orientations were generally within error of one another (archived data and Supplemental Figure S1).

Samples with the highest UCS and Young's modulus include minimally altered granodiorite (Sample 10), silicified samples (6 and 7), and the calcified Sample 5. Silicified samples have the highest compressive strength (up to 286.5 MPa) and Young's modulus (62.8 GPa), and among the lowest Poisson's ratios (0.11-0.13). The strength of the silicified epithermal material is greater than minimally altered granodiorite collected from the Box Canyons site, and six times higher than the weakest altered and damaged samples. The weakest materials contain disseminated chlorite and calcite alteration and a higher percentage of open and partially cemented microfractures.

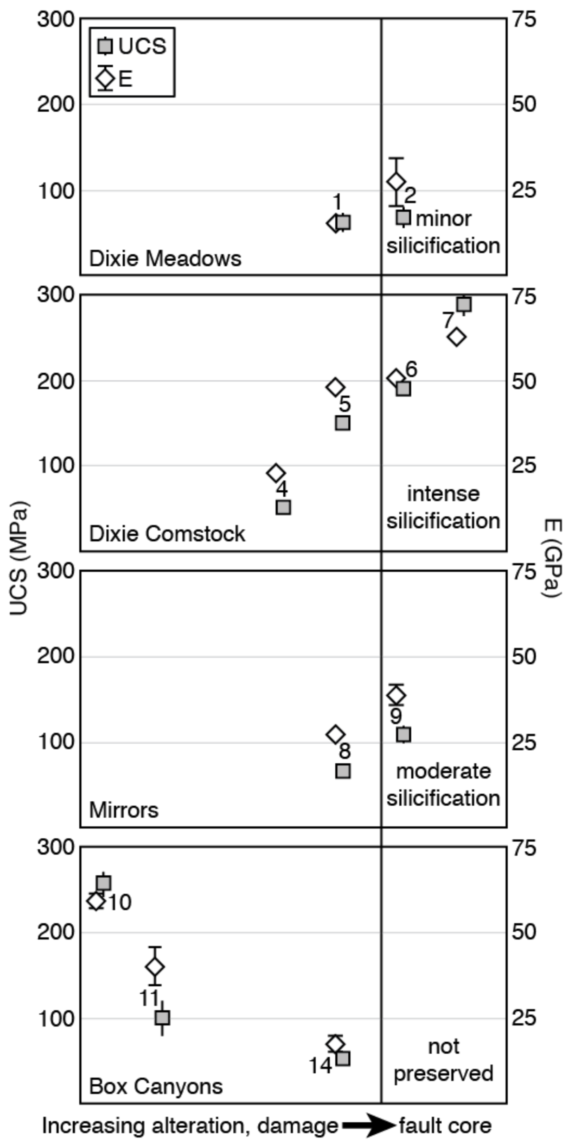

Figure 9. Structural setting, alteration, UCS, and Young's modulus (E) for samples from each site. The Box Canyons site is dominated by increasing fault-proximal damage, resulting in decreased strength, whereas the epithermal environment at Dixie Comstock is associated with silicification of the fault core and significant increases in compressive strength and Young's modulus.

5.2 Fracture Mechanical Properties

We calculated K_{IC} for 13 samples (6-21 specimens per sample) using rapid displacement to total failure (Table 5), and K_{IC}* for 13 samples from 337 plateau loads (6-73 per sample) during slow displacement DT-LR tests (Table 6). Twelve samples were tested for both K_{IC} and K_{IC}*. Despite experimental work indicating loading rate dependence on K_{IC} in some materials (Atkinson & Meredith, 1987), we observed no consistent difference between fracture toughness calculated from rapid or slow displacement tests (Figure 10). The average standard deviation for K_{IC} is 21%. When measurements of K_{IC} are combined with measurements of K_{IC}*, the average standard deviation is reduced to 17%. All figures use K_{IC} from rapid displacement tests unless otherwise noted.

We observed significant variation in K_{IC} between background and more damaged, altered, and cemented fault core and fault proximal material (Figure 11). The highest maximum K_{IC} (3.84 MPa√m) and the highest mean K_{IC} (3.20 MPa√m) were measured in silicified samples from Dixie Comstock. These K_{IC} values are greater than relative pristine granodiorite collected from the Box Canyons site (2.08 MPa√m) and as much as six times higher than the weakest altered and damaged samples (0.56 MPa√m). Moderate silicification (50-60 wt% quartz) in fault core material from the Mirrors is associated with intermediate K_{IC} values similar to unaltered granodiorite. The transect from least altered granodiorite to damage zone samples at the Box Canyons shows a reduction in K_{IC} from >2.0 to <0.7 MPa√m. Similarly altered plutonic rocks from both Dixie Comstock and the Box Canyons, characterized by minor chlorite, calcite, hematite, ±epidote alteration and unhealed damage had similarly low K_{IC} (~0.7 MPa√m). A positive correlation between K_{IC} and UCS (Figure 12) is consistent with the underlying mechanism of failure in UCS tests, microfracture growth and coalescence, which is in turn influenced by K_{IC}.

***Table 5**. K_{IC} from Rapid Displacement DT Testing*

Site	ID	Setting	Fracture Toughness (MPa√m)							
			Minimum	**Q1[a]**	**Median**	**Q3[b]**	**Maximum**	**Mean**	**± std dev**	**n**
DM	**1**	dmg	0.45	1.15	1.25	1.45	1.87	1.24	0.29	21
	2	core	0.75	0.90	1.17	1.47	1.54	1.16	0.31	12
DC	**3**	dmg	0.25	0.55	0.73	0.84	0.95	0.68	0.20	14
	4	dmg	0.30	0.46	0.60	0.66	0.70	0.56	0.13	8
	5	dmg	1.81	1.94	2.13	2.25	2.48	2.12	0.23	7
	6	core	1.84	2.38	2.77	2.93	3.39	2.67	0.44	10
	7	core	2.88	2.93	3.07	3.45	3.84	3.20	0.33	10
M	**8**	dmg	1.86	1.99	2.20	2.33	2.66	2.20	0.27	6
	9	core	1.11	1.92	2.09	2.24	2.47	1.98	0.40	15
BC	**10**	proto	1.53	1.85	2.01	2.27	2.79	2.08	0.32	16
	11	proto	0.33	0.83	0.99	1.22	1.41	1.01	0.26	19
	12	dmg	0.74	0.97	1.12	1.20	1.34	1.07	0.18	10
	13	dmg	-	-	-	-	-	-	-	-
	14	dmg	0.31	0.43	0.62	0.85	1.24	0.67	0.28	11

[a] First quartile. [b] Third quartile.

***Table 6**. K_{IC}* from Fracturing Plateau Loads During DT-LR Tests*

Site	ID	Setting	Peak Stress Intensity (Slow Loading) (MPa√m)							
			Minimum	**Q1**	**Median**	**Q3**	**Maximum**	**Mean**	**± std dev**	**n**
DM	**1**	dmg	1.02	1.11	1.16	1.20	1.31	1.16	0.08	26
	2	core	1.16	1.31	1.46	1.57	2.05	1.46	0.21	16
DC	**3**	dmg	0.22	0.53	0.73	0.90	1.08	0.70	0.27	12
	4	dmg	-	-	-	-	-	-	-	-
	5	dmg	1.04	1.35	1.85	2.01	2.30	1.77	0.39	20

	6	core	2.60	2.90	3.00	3.08	3.49	3.01	0.18	25
	7	core	1.82	2.79	2.93	3.10	3.58	2.94	0.36	21
M	**8**	dmg	1.74	1.90	1.99	2.12	2.43	2.01	0.15	36
	9	core	1.17	1.56	1.84	1.96	2.69	1.79	0.32	73
BC	**10**	proto	1.61	1.81	1.83	2.03	3.07	2.02	0.41	16
	11	proto	0.96	1.09	1.17	1.30	1.45	1.18	0.15	24
	12	dmg	1.23	1.35	1.47	1.56	1.71	1.46	0.16	6
	13	dmg	0.35	0.48	0.51	0.58	0.74	0.53	0.13	13
	14	dmg	0.44	0.54	0.62	0.70	0.79	0.62	0.11	18

We calculated SCI for 13 samples, using 4 to 19 specimens per sample (Table 7). In some tests, induced fractures propagated out of the axial groove, either due to interaction with existing microstructures or improperly balanced loading. These decay curves were not included in SCI calculations. The number of selected decay curves per sample ranged from 1 to 53. The minimum and maximum standard deviations were 23-38%, with an average standard deviation for SCI ~30%. The highest mean SCIs were measured in cemented fault core samples from Dixie Meadows, Dixie Comstock, and the Mirrors (92.3 - 144.6). The Dixie Comstock samples show a systematic increase in SCI with alteration and cementation, from low background values to higher values in the silicified fault core. The range of mean SCI in fault damage zone material is smaller (51.6-76.0). Plots of stress intensity versus velocity (K-V) show 1) fracture propagation at lower stress intensities in weaker material and 2) steeper K-V curves in more altered, fault proximal material with greater microstructural complexity (Figure 11). Calculated fracture growth velocities (Eqs. 2 and 5) are generally between 10^{-5} to 10^{-7} m/s. This range in fracture propagation velocity is similar to values calculated for rocks under ambient conditions by other researchers (Atkinson, 1979a; Wilkins, 1980; Swanson, 1984; Nara & Kaneko, 2005; Chen et al., 2017) and is in part limited by sampling rate and higher signal to noise ratios at slower propagation velocities.

***Table** 7. Subcritical Fracture Growth Index (SCI) from DT-LR Tests*

Site	**ID**	**Setting**	**SCI**							
			Minimum	**Q1**	**Median**	**Q3**	**Maximum**	**Mean**	**± std dev**	**n**
DM	**1**	dmg	15.2	48.1	60.2	68.9	111.6	59.8	21.9	27
	2	core	67.6	77.0	89.5	109.1	122.3	92.9	19.9	6
DC	**3**	dmg	36.8	37.0	50.0	50.9	83.3	51.6	17.0	5
	4	dmg	-	-	-	-	-	-	-	-
	5	dmg	31.8	64.4	74.7	85.3	141.7	74.3	24.8	18
	6	core	54.9	107.0	123.7	145.4	182.9	123.7	31.9	24
	7	core	72.4	114.0	142.9	175.4	202.1	144.7	38.5	15
M	**8**	dmg	39.7	68.0	89.4	110.7	166.5	92.3	31.0	31
	9	core	35.8	68.0	98.2	111.5	172.2	94.4	30.2	53
BC	**10**	proto	34.9	50.5	58.7	65.2	83.8	59.0	13.4	10
	11	proto	43.1	60.9	74.2	89.6	109.4	74.9	18.7	16
	12	dmg	29.1	51.3	64.1	71.2	81.5	60.3	16.8	8

13	dmg	36.5	63.1	70.0	93.0	107.0	75.0	19.1	13
14	dmg	76.0	76.0	76.0	76.0	76.0	76.0	-	1

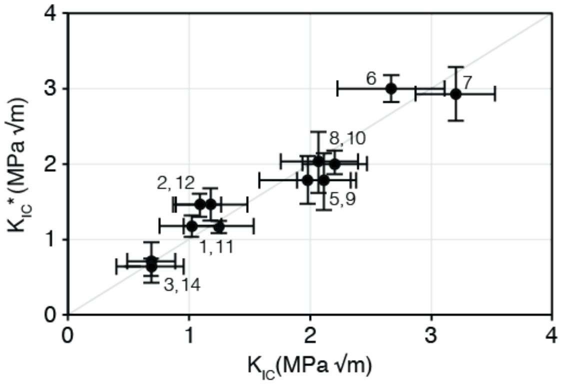

Figure 10. Relationship between K_{IC} and K_{IC}*. Mean K_{IC} and K_{IC}* from rapid and slow displacement tests, respectively, are within error of one another internally and fall along a 1:1 line as a group (Tables 5 & 6). Samples identified by numbers. Sample 13 was not tested with rapid loading and Figures 11-13 show K_{IC}* for this sample. Sample 4 was not tested with slow loading. Error bars are standard deviations of n samples.

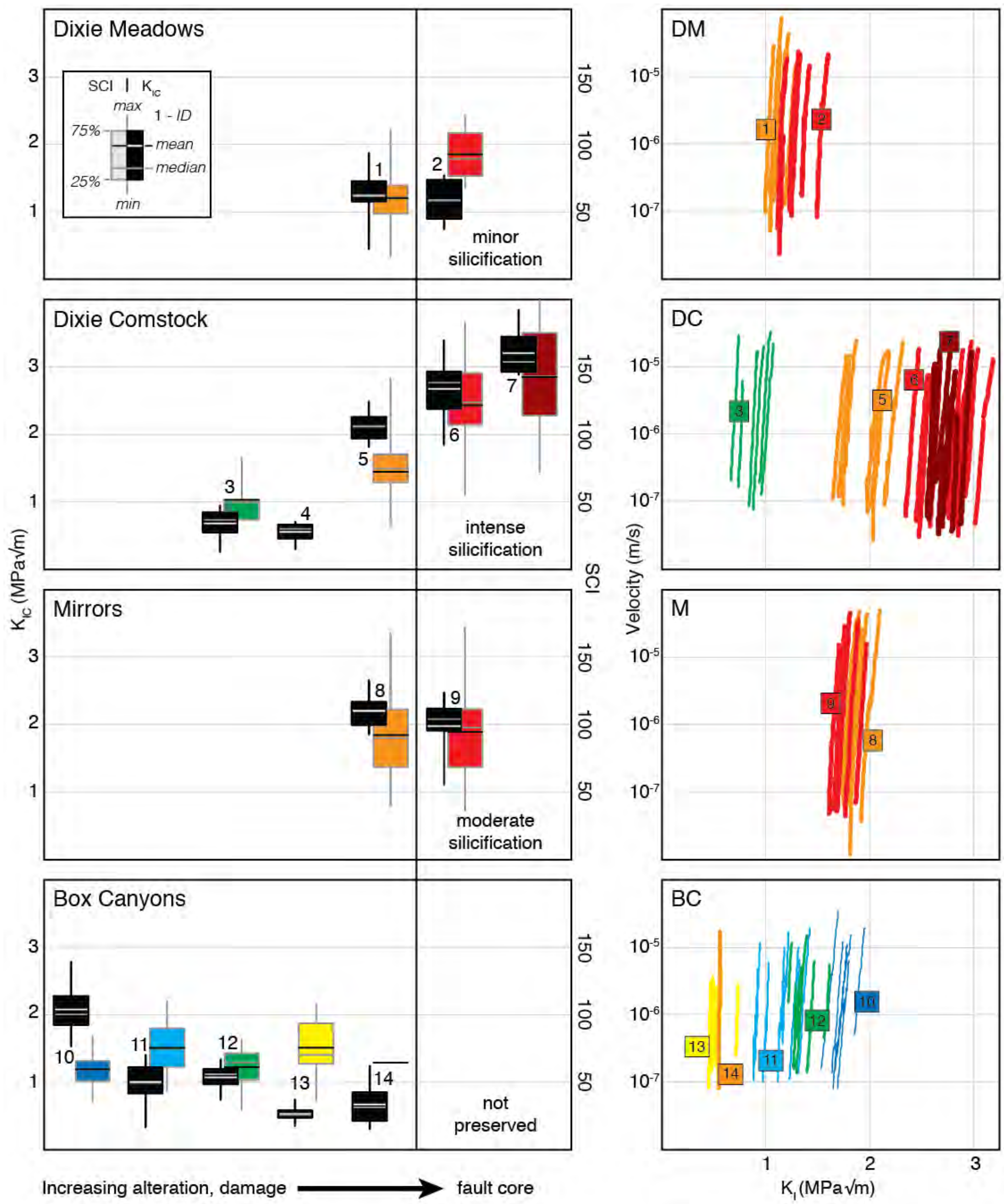

Figure 11. Structural setting, alteration, K_{IC}, SCI, and representative K-V curves for each site. Box plots for K_{IC} and SCI show the complete range of DT test results (Tables 5 & 7). Alteration increases from left to right at each site, with increasing alteration represented by heavier K-V curves and warmer colors. Numbers match sample IDs discussed in the text. K_{IC}* is plotted for Sample 13. Alteration and unhealed damage at the Box Canyons (BC) result in a decrease in toughness, and a subsequent shift left of the

K-V curves. Healing by silicification (±calcite) at the other sites results in an increase in toughness and SCI values in and near the fault core.

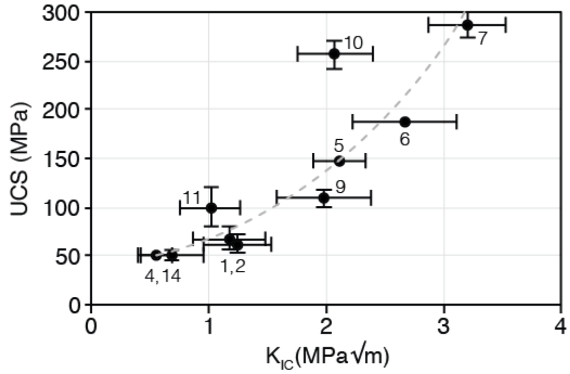

Figure 12. Relationship between K_{IC} and UCS. Positive correlation between mean K_{IC} and mean UCS suggests microfracture growth is an underlying failure mechanism in UCS tests. Samples identified by number. Errors bars show standard deviation of n samples.

6 Discussion

6.1 Mechanical Properties in Altered vs. Pristine Rocks

We observed both increases and decreases in K_{IC}, SCI, UCS, and elastic properties in damaged, altered, and cemented fault zone material. Mean K_{IC} in relatively unaltered granodiorite from the Box Canyons is similar to reported values of K_{IC} from Westerly granite (1.74 MPa√m, Atkinson, 1984; 1.79 ±0.02 MPa√m, Meredith & Atkinson, 1985; 1.43±0.05 MPa√m, Nasseri et al., 2009). SCI is similar to reported values for Lac du Bonnet granodiorite (55.9, 58.5, Wilkins, 1980; 56, Lajtai & Bielus, 1986) and Westerly granite (35.9-39, Atkinson, 1982; 69, Swanson, 1984). However, the most altered and damaged granitic and gabbroic rocks in our dataset show a significant reduction in K_{IC} (<0.7 MPa√m), and silicification resulted in significant increases in mean K_{IC}, SCI, and UCS (up to 3.2 MPa√m, 144.7, and 286.5 MPa, respectively). Silicification at the Dixie Comstock site corresponds to an approximately 600% increase in strength over the weakest footwall samples.

The observed fracture mechanical values in altered and damaged samples are within ranges previous measured in rocks in general (Atkinson, 1984; Swanson, 1984), but rock type is a poor predictor of these properties. K_{IC} in silicified material is similar to both "black gabbro" (2.88 MPa√m, Atkinson, 1984; 2.9 MPa√m, Atkinson, 1982; 2.71-3.03 MPa√m, Meredith & Atkinson, 1985) and quartzite (2.1-2.65 MPa√m, Atkinson, 1984). Novaculite, which is mineralogically similar to the most silicified samples, has less than half of the strength (K_{IC} of 1.335 ±0.075 MPa√m) and lower SCI (25.1) (Atkinson, 1980). These findings suggest that experimental analogs based solely on rock type or mineralogy are likely to be inadequate.

Instead, the reduction in toughness we observed in altered and damaged fault proximal samples is comparable to strength reductions measured in other naturally and experimentally damaged material. Meredith and Atkinson (1985) and Nasseri et al.

(2009) measured reduced K_{IC} in thermally treated Westerly granite containing experimentally induced microfractures. Siratovich et al. (2014) observed a factor of four reduction in UCS with a tripling of connected porosity in volcanic rocks from the Taupo hydrothermal field, New Zealand. Pola et al. (2014) reported a 45-50% reduction in UCS and Young's modulus in altered and weathered samples from dissolution-dominated volcanic environments. Heap et al. (2015) reported a correlation between increasing connected porosity and reduced compressive strength for lava and tuff with different degrees of advanced argillic (acid sulfate) alteration from the White Island volcanically-hosted hydrothermal system, New Zealand.

Despite the occurrence of some degree of damage and alteration in most fault systems, systematic investigations of the impact of alteration on fracture mechanical properties are limited. Atkinson (1984) included a reference to dunite and serpentinized dunite, with serpentinization resulting in a >50% reduction in K_{IC}, from 3.74 to 1.39 MPa√m. Kobayashi et al. (1986) reported low K_{IC} in Ogino tuff (~0.7 MPa√m); the smectite and zeolite altered tuff samples they tested had a lower density, lower UCS, and lower E than the material that we tested, possibly reflecting a greater degree of argillic alteration. Major et al. (2018) reported bleached sandstone from the Crystal Geyser system, Utah, USA, has a lower K_{IC} than adjacent hematite-cemented sandstone.

In the materials that we tested, filling of 85-90% of fracture porosity with mineral cement is associated with a significant increase in all measures of toughness (UCS, K_{IC}, SCI) (Figure 13). The observation that damaged rocks can regain significant strength and resistance to fracture growth is consistent with other researchers that observed strengthening resulting from mineral precipitation (quartz, Yasuhara, 2005; alunite, del Potro & Hürlimann, 2009, and Heap et al., 2015; phyllosilicate and calcite, Boulton et al., 2017; hematite and calcite, Major et al., 2018). Our sample base is too small to address the differences in strength recovery resulting from specific fracture cement composition, texture, or distribution. However, the addition of fracture-filling mineral cements in particular hydrothermal settings will clearly impact the distribution of rock strength in hydrothermal systems.

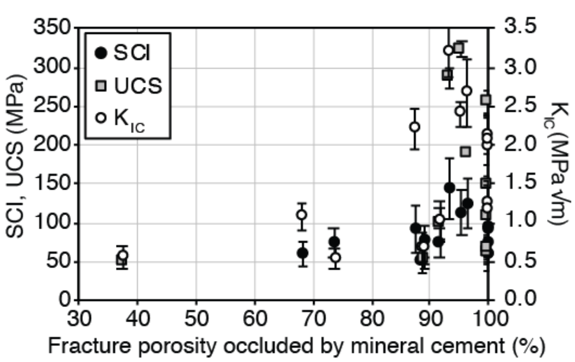

Figure 13. Mechanical properties and fracture fill. Abundant open microfractures results in mechanically weak samples. Cementation, indicated by reduction of remnant fracture porosity to <15%, results in substantial increases in K_{IC}, SCI, and UCS.

6.2 Implications for Strength Distribution in Fault-Hosted Hydrothermal Systems

Just as hydrothermal systems commonly contain systematic spatial variations in alteration products related to temperature, fluid chemistry, and fluid-rock ratios (Simmons et al., 2005; Tosdal et al., 2009; Nishimoto & Yoshida, 2010; Sillitoe, 2010), the spatial distribution of mechanical properties in and around fault-fracture conduits is expected to change with the dominant alteration mechanism and from competition between the accumulation of damage versus healing. Where precipitation of strong minerals outpaces deformation, fault rocks will experience interseismic strengthening. Conversely, regions with a lower rate of mineral precipitation relative to deformation will tend to undergo progressive weakening. A comparison of the Dixie Comstock and Box Canyons results suggests a depth-dependent inversion between the mechanical properties of fault rocks and host rocks in fault-hosted hydrothermal systems (Figure 14). In the shallow, precipitation-dominated epithermal setting at Dixie Comstock, samples from the thick, silicified fault core are up to six times stronger than chloritized footwall samples and more resistant to fracture growth. The exhumed chlorite-calcite-hematite assemblage preserved at the Box Canyons shows a reduction in UCS and K_{IC} near the fault. The reduction in fracture mechanical properties with depth, in particular, could be exacerbated by increasing temperature and changes in fluid chemistry (Atkinson, 1979a; Atkinson & Meredith, 1981; Meredith & Atkinson, 1985; Karfakis & Akram, 1993; Balme et al., 2004; Funatsu et al., 2004; Rostom et al., 2012; Nara et al., 2013, 2014, 2017). However, chemically aided fracture growth is sensitive to rock composition, and has not been thoroughly characterized in similarly altered fault rocks.

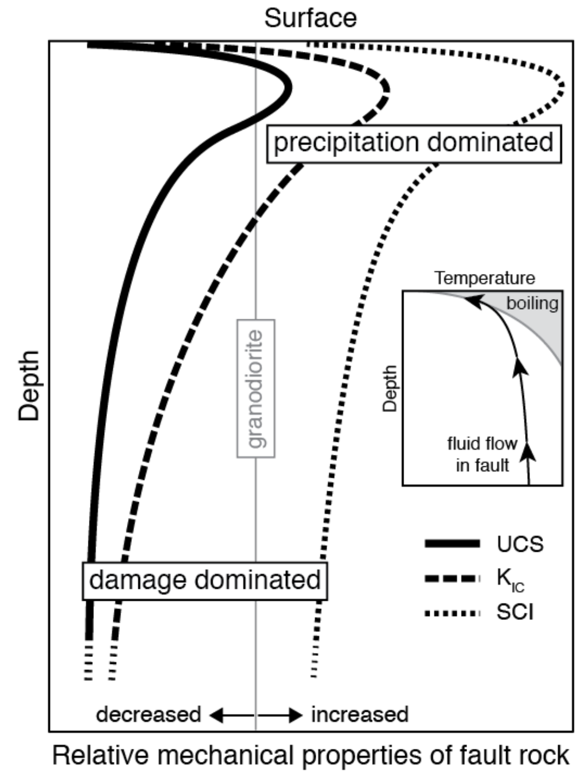

Figure 14. Schematic mechanical properties with depth in a fault hosting advective, high temperature fluid flow. Inset shows upward migration of fluid, boiling, and rapid cooling, resulting in mineral precipitation. Measures of strength and resistance to fracture propagation (UCS, K_{IC}, SCI) are generally lower in the fault core than in adjacent rock, but in shallow, precipitation dominated hydrothermal regimes cementation of the fault core by silicification (±calcification) increases rock strength relative to less cemented damage zone and protolith. Increased dissolution in the near surface acid sulfate environment is associated with a loss of strength.

The distribution of mechanical properties with depth in hydrothermal systems may have implications for fault zone architecture and hydraulic properties. In portions of hydrothermal systems dominated by dissolution and the accumulation of unhealed damage, we expect deformation to become increasingly localized. In contrast, rapid advection, cooling, and enhanced precipitation in shallow portions of fault-hosted hydrothermal systems, where conditions approach the boiling point with depth curve (Figures 2, 14), may inhibit fracture growth in the primary conduits and promote fracture growth in adjacent material, ultimately contributing to large volumes of fractured rock and distributed alteration in shallow portions of these systems.

6.3 Broader Impacts of Alteration, Damage, and Healing

Hydrothermal alteration and the preservation or healing of damage impacts several other geologic systems of particular interest to society, including mineral deposits, volcano-magmatic systems, and fault systems more generally. Moir et al. (2013) showed that dilatant damage around mineralized fault zones could be related to contrasting mechanical properties in different host lithologies, a correlation which was also observed around the Alpine Fault in New Zealand (Williams et al., 2016). Our results suggest that the distribution of fracture strength parameters, fracture growth, and fracture permeability may be heterogeneous in both space and time around mineralizing faults due to mechanical changes resulting from hydrothermal alteration. Rock weakening caused by acid sulfate and argillic alteration in volcanic edifices is linked to flank collapse (Lopez & Williams, 1993; Watters et al., 2000; Reid et al., 2001; del Potro & Hürlimann, 2009). However, cementation by quartz or alunite in these environments may result in local densification and strengthening, with physical and mechanical contrast between different alteration products potentially influencing where flank collapse ultimately occurs. Opening-mode fractures are fundamental parts of fault initiation in crystalline rock (Crider, 2015) and persistent elements in damage zones in mature fault systems (Wilson et al., 2003; Davatzes et al., 2005). Subcritical fracture growth in damage zones has been implemented in pre-and post-seismic behavior of fault systems (Anderson & Grew, 1977; Rudnicki, 1980; Brantut et al., 2013). However, because some degree of hydrothermal alteration is common in large seismogenic faults (e.g. Parry et al., 1991; Bruhn et al., 1994), geomechanical tests of pristine material alone may not completely characterize the fracture mechanical properties of fault zones. The existence of a healing threshold, where sealing of 85-90% fractures results in a significant increase in material strength in our samples, has been documented in other fault settings (e.g. Williams et al., 2016) and may represent a useful approximation of strength recovery in faults and hydrothermal systems.

7 Conclusions

We combined unconfined compressive strength tests, mineralogical and textural characterization, and double-torsion load-relaxation fracture mechanics tests to measure strength, elastic, and fracture mechanical properties in exhumed suites of rocks from different hydrothermal alteration regimes preserved in the footwall of the Dixie Valley – Stillwater fault zone. The alteration regimes include 1) a shallow acid sulfate regime dominated by quartz and calcite precipitation, 2) an epithermal regime dominated by intense silicification after earlier sodic and calcic alteration, 3) a moderate depth and temperature silicic-argillic regime dominated by quartz, kaolinite, and carbonates, and 4) a retrograde alteration regime dominated by chlorite-calcite-hematite assemblages and unhealed damage. Based on the alteration assemblages that we tested, the mechanical contrast between fault core and host rocks changes between precipitation- vs damage-dominated regimes. Compared to minimally altered granodiorite, silicified fault rocks are stronger and more resistant to fracture growth, whereas fault damage zone samples containing chlorite-calcite-hematite alteration and abundant unhealed fractures are one third to one fifth as strong. Sealing of >85-90% of microfracture porosity by quartz and/or calcite in the fault zone in the epithermal environment is associated with a significant increase in UCS, K_{IC}, and SCI above values of altered protolith in the footwall. The mechanical properties that we measured in altered, damaged, and healed fault zone samples are not readily predicted from geomechanical tests of pristine rocks.

Acknowledgments, Samples, and Data

Donnie Brooks assisted with rock mechanics testing at the Rock Mechanics Lab, Bureau of Economic Geology, Austin, TX. Xiaofeng Chen improved the double-torsion testing apparatus, method, and data reduction routine. Jonathan Major helped with sample preparation and XRD analysis. Sol Cooperdock, Alison MacNamee, and Adenike Tokan-Lawal provided field assistance. Whitney Behr provided feedback on an early version of this manuscript. We thank JGR reviewers Michael J. Allen and John Bedford for their helpful comments. Funding was provided by grants from The GDL Foundation, The Geothermal Resources Council, and The American Association of Petroleum Geologists Foundation. Additional support was provided by The Jackson School of Geosciences and the Fracture Research and Application Consortium (FRAC) at The University of Texas at Austin. Sample information and supporting data are archived at http://www.geosamples.org and http://dx.doi.org/10.17632/dpphj7z94g.1. The authors have no real or perceive conflicts of interest. Publication authorized by the Director, Bureau of Economic Geology.

References

Allen, M. J., Tatham, D., Faulkner, D. R., Mariani, E., & Boulton, C. (2017). Permeability and seismic velocity and their anisotropy across the Alpine Fault, New Zealand: an insight from laboratory measurements on core from the Deep Fault Drilling Project phase 1 (DFDP-1). Journal of Geophysical Research - Solid Earth, 122, 6160-6179. https://www.doi.org/10.1002/2017JB014355.

Anders, M. H., Schneider, J. R., Scholz, C. H., & Losh, S. (2013). Mode I microfracturing and fluid flow in damage zones: the key to distinguishing faults from slides. *Journal of Structural Geology, 48*, 113-125. https://doi.org/10.1016/j.jsg.2012.11.010

Anderson, O. L., & Grew, P. C. (1977). Stress corrosion theory of crack propagation with applications to geophysics. *Review of Geophysics and Space Physics, 15*(1), 77-104. https://doi.org/10.1029/RG015i001p00077

Atkinson, B. K. (1979a). A fracture mechanics study of subcritical tensile cracking of quartz in wet environments. *Pure and Applied Geophysics, 117*, 1011-1024. https://doi.org/10.1007/BF00876082

Atkinson, B. K. (1979b). Technical note: fracture toughness of Tennessee sandstone and Carrara marble using the double torsion testing method. *Int J Rock Mech Min Sci & Geomech, 16*, 49-53. https://doi.org/10.1016/0148-9062(79)90513-8

Atkinson, B. K., & Meredith, P. G. (1981). Stress corrosion cracking of quartz: a note on the influence of chemical environment. *Tectonophysics, 77*, T1-T11. https://doi.org/10.1016/0040-1951(81)90157-8

Atkinson, B. K. (1980). Stress corrosion and the rate-depedent tensile failure of a fine-grained quartz rock. *Tectonophysics, 65*, 281-290. https://doi.org/10.1016/0040-1951(80)90078-5

Atkinson, B. K. (1982). Subcritical crack propagation in rocks: theory, experimental results and applications. *Journal of Structural Geology, 4*(1), 41-56. https://doi.org/10.1016/0191-8141(82)90005-0

Atkinson, B. K. (1984). Subcritical crack growth in geological materials. *Journal of Geophysical Research, 89*(B6), 4077. https://doi.org/10.1029/JB089iB06p04077

Atkinson, B. K., & Meredith, P. G. (1987). Experimental fracture mechanics data for rocks and minerals. In B. K. Atkinson (Ed.), *Fractures Mechanics of Rock* (pp. 477-525). London: Academic Press. https://doi.org/10.1016/0148-9062(88)91866-9

Balme, M. R., Rocchi, V., Jones, C., Sammonds, P. R., Meredith, P. G., & Boon, S. (2004). Fracture toughness measurements on igneous rocks using a high-pressure, high-temperature rock fracture mechanics cell. *Journal of Volcanology and Geothermal Research, 132*(2-3), 159-172. https://doi.org/10.1016/s0377-0273(03)00343-3

Bell, J. W., Caskey, S. J., Ramelli, A. R., & Guerrieri, L. (2004). Pattern and rates of faulting in the Central Nevada Seismic Belt, and paleoseismic evidence for prior beltlike behavior. *Bulletin of the Seismological Society of America, 94*(4), 1229-1254. http://doi.org/10.1785/012003226

Bell, J. W., & Katzer, T. (1990). Timing of late Quaternary faulting in the 1954 Dixie Valley earthquake area, central Nevada. *Geology, 18*(7), 622. https://doi.org/10.1130/0091-7613(1990)018<0622:tolqfi>2.3.co;2

Benoit, D. (1992). A case history of injection through 1991 at Dixie Valley, Nevada. GRC Transactions, 16, 611-620. https://www.geothermal-library.org/index.php?mode=pubs&action=view&record=1002254

Benoit, D. (2015). A case history of the Dixie Valley Geothermal Field, 1963-2014. GRC Transactions, 39, 3-12. https://www.geothermal-library.org/index.php?mode=pubs&action=view&record=1032128

Berkowitz, B. (2002). Characterizing flow and transport in fractured geological media: a review. *Advances in Water Resources, 25*, 861-884. https://doi.org/10.1016/S0309-1708(02)00042-8

Berry, G. W., Grim, P. J., & Ikelman, J. A. (1980). *Thermal springs list for the United States*. Springfield, Virginia: NOAA/EDIS Retrieved from https://www.osti.gov/biblio/6737326.

Blackwell, D. D., Golan, B., & Benoit, D. (2000). Temperatures in the Dixie Valley, Nevada geothermal system. *GRC Transactions, 24*, 223-228. https://www.geothermal-library.org/index.php?mode=pubs&action=view&record=1016796

Blackwell, D. D., Smith, R. P., & Richards, M. C. (2007). *Exploration and development at Dixie Valley, Nevada: summary of DOE studies*. Paper presented at the 32nd Workshop on Geothermal Reservoir Engineering, Stanford University, Stanford, California. https://www.geothermal-library.org/index.php?mode=pubs&action=view&record=8005099

Blenkinsop, T. G. (2008). Relationships between faults, extension fractures and veins, and stress. *Journal of Structural Geology, 30*(5), 622-632. https://www.doi.org/10.1016/j.jsg.2008.01.008

Boulton, C., Menzies, C. D., Toy, V. G., Townend, J., & Sutherland, R. (2017). Geochemical and microstructural evidence for interseismic changes in fault zone permeability and strength, Alpine Fault, New Zealand. *Geochemistry, Geophysics, Geosystems, 18*, 238-265. https://www.doi.org/10.1002/2016GC006588

Brantut, N., Heap, M. J., Meredith, P. G., & Baud, P. (2013). Time-dependent cracking and brittle creep in crustal rocks: a review. *Journal of Structural Geology, 52*, 17-43. https://www.doi.org/10.1016/j.jsg.2013.03.007

Brown, S. R., & Bruhn, R. L. (1996). Formation of voids and veins during faulting. *Journal of Structural Geology, 18*(5), 657-671. https://doi.org/10.1016/S0191-8141(96)80031-9

Brown, W. F., & Strawley, J. E. (1966). *Plane strain crack toughness testing of high strength metallic materials, ASTM STP 410*. https://www.doi.org/10.1520/STP410-EB

Browne, P. R. L. (1978). Hydrothermal alteration in active geothermal fields. *Annual Review of Earth and Planetary Sciences, 6*, 229-250. https://doi-org.ezproxy.lib.utexas.edu/10.1146/annurev.ea.06.050178.001305

Bruhn, R. L., Parry, W. T., Yonkee, W. A., & Thompson, T. (1994). Fracturing and hydrothermal alteration in normal fault zones. *Pure and Applied Geophysics, 142*(3/4), 609-644. https://www.doi.org/10.1007/BF00876057

Caine, J. S., Bruhn, R. L., & Forster, C. B. (2010). Internal structure, fault rocks, and inferences regarding deformation, fluid flow, and mineralization in the seismogenic Stillwater normal fault, Dixie Valley, Nevada. *Journal of Structural Geology, 32*(11), 1576-1589. https://www.doi.org/10.1016/j.jsg.2010.03.004

Caine, J. S., Evans, J. P., & Forster, C. B. (1996). Fault zone architecture and permeability structure. *Geology, 24*(11), 1025-1028. https://www.doi.org/10.1130/0091-7613(1996)024<1025:fzaaps>2.3.co;2

Callahan, O., (2019). Data in support of "Fracture Mechanical Properties of Damaged and Hydrothermally Altered Rocks, Dixie Valley - Stillwater Fault Zone, Nevada, USA" by Owen A. Callahan, Peter Eichhubl, Jon E. Olson, and Nicholas C. Davatzes, Mendeley Data, v1. http://dx.doi.org/10.17632/dpphj7z94g.1

Caskey, S. J., Wesnousky, S. G., Zhang, P., & Slemmons, D. B. (1996). Surface faulting of the 1954 Fairview Peak (Ms 7.2) and Dixie Valley (Ms 6.8) earthquakes, central Nevada. *Bulletin of the Seismological Society of America, 86*(3), 761-787.

Caskey, J. S., Bell, J. W., Ramelli, A. R., & Wesnousky, S. G. (2004). Historic surface faulting and paleoseismicity in the area of the 1954 Rainbow Mountain-Stillwater earthquake sequence, central Nevada. *Bulletin of the Seismological Society of America, 94*(4), 1255-1275. https://doi.org/10.1785/012003012

Chen, X., Eichhubl, P., & Olson, J. E. (2017). Effect of water on critical and subcritical fracture properties of Woodford shale. *Journal of Geophysical Research - Solid Earth, 122*, 2736-2750. https://doi.org/10.1002/2016JB013708

Crafford, A. E. J. (2007). Geologic Map of Nevada: U.S. Geological Survey Data Series 249. Retrieved 11-25-2009 https://pubs.usgs.gov/ds/2007/249/

Crider, J. G. (2015). The initiation of brittle faults in crystalline rock. *Journal of Structural Geology, 77*, 159-174. https://doi.org/10.1016/j.jsg.2015.05.001

Davatzes, N. C., & Aydin, A. (2003). Overprinting faulting mechanisms in high porosity sandstones of SE Utah. *Journal of Structural Geology, 25*(11), 1795-1813. https://doi.org/10.1016/s0191-8141(03)00043-9

Davatzes, N. C., Aydin, A., & Eichhubl, P. (2003). Overprinting faulting mechanisms during the development of multiple fault sets in sandstone, Chimney Rock fault array, Utah, USA. *Tectonophysics, 363*(1-2), 1-18. https://doi.org/10.1016/s0040-1951(02)00647-9

Davatzes, N. C., Eichhubl, P., & Aydin, A. (2005). Structural evolution of fault zones in sandstone by multiple deformation mechanisms; Moab Fault, southeast Utah. *Geological Society of America Bulletin, 117*(1-2), 135-148. https://doi.org/10.1130/b25473.1

del Potro, R., & Hürlimann, M. (2009). The decrease in the shear strength of volcanic materials with argillic hydrothermal alteration, insights from the summit region of Teide stratovolcano, Tenerife. *Engineering Geology, 104*(1-2), 135-143. https://doi.org/10.1016/j.enggeo.2008.09.005

Dilek, Y., & Moores, E. M. (1995). Geology of the Humboldt igneous complex, Nevada, and tectonic implications for the Jurassic magmatism in the Cordilleran orogen. In D. M. Miller & C. Busby (Eds.), *Jurassic Magmatism and Tectonics of the North American Cordillera* (pp. 229-248). Boulder, Colorado: Geological Society of America Special Paper 299. https://www.doi.org/10.1130/SPE299-p229

Eichhubl, P., Davatzes, N. C., & Becker, S. P. (2009). Structural and diagenetic control of fluid migration and cementation along the Moab fault, Utah. *AAPG Bulletin, 93*(5), 653-681. https://doi.org/10.1306/02180908080

Eichhubl, P., Taylor, W. L., Pollard, D. D., & Aydin, A. (2004). Paleo-fluid flow and deformation in the Aztec Sandstone at the Valley of Fire, Nevada; evidence for the coupling of hydrogeologic, diagenetic, and tectonic processes. *Geological Society of America Bulletin, 116*(9-10), 1120-1136. https://doi.org/10.1130/b25446.1

Engelder, T., Fischer, M. P., & Gross, M. R. (1993). *GSA Short Course Notes: Geological Aspects of Fracture Mechanics*. Boston, MA: GSA Division of Structural Geology and Tectonics.

Evans, A. G. (1972). A method for evaluating the time-dependent failutre characteristics of brittle materials - and its application to polycrystalline alumina. *Journal of Materials Science, 7*, 1137-1146. https://doi.org/10.1007/BF00550196

Facca, G., & Tonani, F. (1967). The self-sealing geothermal field. *Bulletin Volcanologique, 30*(1), 271-273. https://doi.org/10.1007/BF02597674

Fuller, E. R. (1979). An evaluation of double-torsion testing - analysis. In S. W. Freiman (Ed.), *Fracture Mechanics Applied to Brittle Materials, ASTM STP 678* (pp. 3-18): American Society for Testing and Materials. https://doi.org/10.1520/STP36621S.

Funatsu, T., Seto, M., Shimada, H., Matsui, K., & Kuruppu, M. (2004). Combined effects of increasing temperature and confining pressure on the fracture toughness of clay bearing rocks. *International Journal of Rock Mechanics and Mining Sciences, 41*(6), 927-938. https://www.doi.org/10.1016/j.ijrmms.2004.02.008

Haas, J. L., Jr. (1971). The effect of salinity on the maximum thermal gradient of a hydrothermal system at hydrostatic pressure. *Economic Geology and the Bulletin of the Society of Economic Geologists, 66*(6), 940-946. https://doi.org/10.2113/gsecongeo.66.6.940

Heap, M. J., Kennedy, B. M., Pernin, N., Jacquemard, L., Baud, P., Farquharson, J. I., et al. (2015). Mechanical behaviour and failure modes in the Whakaari (White Island volcano) hydrothermal system, New Zealand. *Journal of Volcanology and Geothermal Research, 295*, 26-42. https://doi.org/10.1016/j.jvolgeores.2015.02.012

Henley, R. W., & Ellis, A. J. (1983). Geothermal systems ancient and modern: a geochemical review. *Earth-Science Reviews, 19*, 1-50. https://doi.org/10.1016/0012-8252(83)90075-2

Hillier, S. (1999). Use of an air brush to spray dry samples for X-ray powder diffraction. *Clay Minerals, 34*, 127-135. https://www.doi.org/10.1180/000985599545984

Holder, J., Olson, J. E., & Philip, Z. (2001). Experimental determination of subcritical crack growth parameters in sedimentary rock. *Geophysical Research Letters, 28*(4), 599-602. https://doi.org/10.1029/2000GL011918

John, D. A. (1995). Tilted middle Tertiary ash-flow calderas and subjacent granitic plutons, southern Stillwater Range, Nevada: cross sections of an Oligocene igneous center. *GSA Bulletin, 107*(2), 180-200. https://doi.org/10.1130/0016-7606(1995)107<0180:TMTAFC>2.3.CO;2

Johnson, D. A., & Barton, M. D. (2000). Time-space development of an extern brine-dominated, igneous-driven hydrothermal system: Humboldt Mafic Compex, Western Nevada, Part I. In J. H. Dilles, M. D. Barton, D. A. Johnson, J. M. Proffett, & M. T. Einaudi (Eds.), *Contrasting styles of intrusion-associated hydrothermal systems* (Vol. 32, pp. 127-143): Society of Economic Geologists. https://doi.org/10.5382/GB.32

Karfakis, M. G., & Akram, M. (1993). Effects of chemical solutions on rock fracturing. *International Journal of Rock Mechanics & Mining Sciences, 30*(7), 1253-1259. https://doi.org/10.1016/0148-9062(93)90104-L

Kennedy-Bowdoin, T., Silver, E. A., Martini, B. A., & Pickles, W. L. (2004). Geothermal prospecting using hyperspectral imaging and field observations, Dixie Meadows, NV. *GRC Transactions*, 10.

Kistler, R. W., & Speed, R. C. (2000). $^{40}Ar/^{39}Ar$, K-Ar, Rb-Sr whole rock and mineral ages, chemical composition, strontium, oxygen and hydrogen isotopic systematics of Jurassic Humboldt Lopolith and Permian (?) and Triassic Koipato Group rocks, Pershing and Churchill Counties, Nevada. USGS Open File Report 00-217. https://doi.org/10.3133/ofr00217

Kobayashi, R., Matsuki, K., & Otsuka, N. (1986). Size effect in the fracture toughness of Ogino Tuff. *Int J Rock Mech Min Sci & Geomech, 23*, 13-18. https://doi.org/10.1016/0148-9062(86)91662-1

Lajtai, E. Z., & Bielus, L. P. (1986). Stress corrosion cracking of Lac du Bonnet Granite in tension and compression. *Rock Mechanics and Rock Engineering, 19*, 71-87. https://doi.org/10.1007/BF01042525

Lamb, A., Kratt, C., & Calvin, W. (2011). Geothermal exploration using hyperspectral analysis over Dixie and Fairview Valleys, Nevada. *GRC Transactions, 35*, 867-871. https://www.geothermal-library.org/index.php?mode=pubs&action=view&record=1029344

Lopez, D. L., & Williams, S. N. (1993). Catastrophic volcanic collapse: relation to hydrothermal processes. *Science, 260*(5115), 1794-1796. https://doi.org/10.1126/science.260.5115.1794

Lowell, R. P., van Cappellen, P., & Germanovich, L. N. (1993). Silica precipitation in fractures and the evolution of permeability in hydrothermal upflow zones. *Science, 260*(5105), 192-194. https://www.doi.org/10.1126/science.260.5105.192

Lutz, S. J., & Moore, J. M. (1996). Alteration mineralogy of the Dixie Valley Geothermal System, Nevada. *GRC Transactions, 20*, 353-362. https://www.geothermal-library.org/index.php?mode=pubs&action=view&record=1014756

Lutz, S. J., Caskey, S. J., Mildenhall, D. D., Browne, P. R. L., & Johnson, S. D. (2002). *Dating sinter deposits in northern Dixie Valley, Nevada-the paleoseismic record and implications for the Dixie Valley geothermal system*. Paper presented at the 27th Workshop on Geothermal Reservoir Engineering, Stanford University. https://www.geothermal-library.org/index.php?mode=pubs&action=view&record=1017549

Major, J. R., Eichhubl, P., Dewers, T. A., & Olson, J. E. (2018). Effect of CO_2–brine–rock interaction on fracture mechanical properties of CO_2 reservoirs and seals. *Earth and Planetary Science Letters, 499*, 37-47. https://doi.org/10.1016/j.epsl.2018.07.013

Meredith, P. G., & Atkinson, B. K. (1985). Fracture toughness and subcritical crack growth during high-temperature deformation of Westerly granite and Black gabbro. *Physics of the Earth and Planetary Interiors, 39*, 33-51. https://doi.org/10.1016/0031-9201(85)90113-X

Moir, H., Lunn, R. J., Micklethwaite, S., & Shipton, Z. K. (2013). Distant off-fault damage and gold mineralization: the impact of rock heterogeneity. *Tectonophysics, 608*, 461-467. https://doi.org/10.1016/j.tecto.2013.08.043

Moore, D. E., Morrow, C. A., & Byerlee, J. D. (1983). Chemical reactions accompanying fluid flow through granite held in a temperature gradient. *Geochimica et Cosmochimica Acta, 47*(3), 445-453. https://doi.org/10.1016/0016-7037(83)90267-3

Nara, Y., & Kaneko, K. (2005). Study of subcritical crack growth in andesite using the double torsion test. *International Journal of Rock Mechanics & Mining Sciences, 42*, 521-530. https://doi.org/10.1016/j.ijrmms.2005.02.001

Nara, Y., Kashiwaya, K., Nishida, Y., & Ii, T. (2017). Influence of surrounding environment on subcritical crack growth in marble. *Tectonophysics, 706-707*, 116-128. https://doi.org/10.1016/j.tecto.2017.04.008

Nara, Y., Morimoto, K., Hiroyoshi, N., Yoneda, T., Kaneko, K., & Benson, P. M. (2012). Influence of relative humidity on fracture toughness of rock: implications for subcritical crack growth. *International Journal of Solids and Structures, 49*, 2471-2481. https://doi.org/10.1016/j.ijsolstr.2012.05.009

Nara, Y., Nakabayashi, R., Maruyama, M., Hiroyoshi, N., Yoneda, T., & Kaneko, K. (2014). Influences of electrolyte concentration on subcritical crack growth in sandstone in water. *Engineering Geology, 179*, 41-49. https://doi.org/10.1016/j.enggeo.2014.06.018

Nara, Y., Yamanaka, H., Oe, Y., & Kaneko, K. (2013). Influence of temperature and water on subcritical crack growth parameters and long-term strength for igneous rocks. *Geophysical Journal International, 193*(1), 47-60. https://doi.org/10.1093/gji/ggs116

Nasseri, M. H. B., Tatone, B. S. A., Grasselli, G., & Young, R. P. (2009). Fracture toughness and fracture roughness interrelationship in thermally treated Westerly Granite. *Pure and Applied Geophysics, 166*(5-7), 801-822. https://doi.org/10.1007/s00024-009-0476-3

Nelson, E. P., Kullman, A. J., Gardner, M. H., & Batzle, M. (1999). Fault-fracture networks and related fluid flow and sealing, Brushy Canyon Formation, west Texas. In W. C. Haneberg, P. S. Mozley, J. C. Moore, & L. B. Goodwin (Eds.), *Faults and Subsurface Fluid Flow in the Shallow Crust* (Vol. 113, pp. 69-81). Washington, D.C.: American Geophysical Union. https://www.doi.org/10.1029/GM113p0069

Nishimoto, S., & Yoshida, H. (2010). Hydrothermal alteration of deep fractured granite: effects of dissolution and precipitation. *Lithos, 115*(1-4), 153-162. https://doi.org/10.1016/j.lithos.2009.11.015

NREL. (2016). Geothermal Prospector. Retrieved from https://maps.nrel.gov/geothermal-prospector

Okaya, D. A., & Thompson, G. A. (1985). Geometry of Cenozoic extensional faulting: Dixie Valley, Nevada. *Tectonics, 4*(1), 107-125. https://doi.org/10.1029/TC004i001p00107

Olson, J. E. (1993). Joint pattern development: effects of subcritical crack growth and mechanical crack interaction. *Journal of Geophysical Research, 98*(B7), 12,251-212,265. https://www.doi.org/10.1029/93JB00779

Olson, J. E. (2004). Predicting fracture swarms - the influence of subcritical crack growth and the crack-tip process zone on joint spacing in rock. In J. W. Cosgrove & T. Engelder (Eds.), *The initiation, propagation, and arrest of joints and other fractures* (Vol. 231, pp. 73-88). London: Geological Society. https://doi.org/10.1144/gsl.sp.2004.231.01.05

Page, B. M. (1965). Preliminary geologic map of a part of the Stillwater Range, Churchill County, Nevada. Nevada Bureau of Mines, Map 28. 1;125,000. http://data.nbmg.unr.edu/public/freedownloads/m/m028.zip

Parry, W. T., & Bruhn, R. L. (1990). Fluid pressure transients on seismogenic normal faults. *Tectonophysics, 179*, 335-344. https://doi.org/10.1016/0040-1951(90)90299-N

Parry, W. T., Hedderly-Smith, D., & Bruhn, R. L. (1991). Fluid inclusions and hydrothermal alteration on the Dixie Valley Fault, Nevada. *Journal of Geophysical Research, 96*(B12), 19733. https://doi.org/10.1029/91jb01965

Pletka, B. J., Fuller, E. R., Jr., & Koepke, B. G. (1979). An evaluation of double-torsion testing - experimental. In S. W. Freiman (Ed.), *Fracture Mechanics Applied to Brittle Materials, ASTM STP 678* (pp. 19-37): American Society for Testing and Materials. https://www.doi.org/10.1520/STP36622S

Pola, A., Crosta, G. B., Fusi, N., & Castellanza, R. (2014). General characterization of the mechanical behaviour of different volcanic rocks with respect to alteration. *Engineering Geology, 169*, 1-13. https://doi.org/10.1016/j.enggeo.2013.11.011

Power, W. L., & Tullis, T. E. (1989). The relationship between slickenside surface in fine-grained quartz and the seismic cycle. *Journal of Structural Geology, 11*(7), 879-893. https://doi.org/10.1016/0191-8141(89)90105-3

Power, W. L., & Tullis, T. E. (1992). The contact between opposing fault surfaces at Dixie Valley, Nevada, and implications for fault mechanics. *Journal of Geophysical Research, 97*(B11), 15425. https://doi.org/10.1029/92jb01059

Reid, M. E., Sisson, T. W., & Brien, D. L. (2001). Volcano collapse promoted by hydrothermal alteration and edifice shape, Mount Rainier, Washington. *Geology, 29*(9), 779-782. https://doi.org/10.1130/0091-7613(2001)029<0779:VCPBHA>2.0.CO;2

Rostom, F., Royne, A., Dysthe, D. K., & Renard, F. (2012). Effect of fluid salinity on subcritical crack propagation in calcite. *Tectonophysics, 583*, 68-75. https://www.doi.org/10.1016/j.tecto.2012.10.023

Rudnicki, J. W. (1980). Fracture mechanics applied to the earth's crust. *Annual Review of Earth and Planetary Sciences, 8*, 489-525. https://doi.org/10.1146/annurev.ea.08.050180.002421

Sano, O., Kudo, Y., & Mizuta, Y. (1992). Experimental determination of elastic constants of Oshima granite, Barre granite, and Chelmsford granite. *Journal of Geophysical Research - Solid Earth, 97*(B3), 3367-3379. https://doi.org/10.1029/91jb02934

Schwering, P. C. (2013). *Geophysical modeling of the Dixie Meadows Geothermal prospect: dual analysis of gravity and magnetic data towards identifying structural controls.* (M.S.), University of Nevada, Reno, University of Nevada, Reno.

Seront, B., Wong, T.-F., Caine, J. S., Forster, C. B., Bruhn, R., L., & Fredrich, J. T. (1998). Laboratory characterization of hydromechanical properties of a seismogenic normal fault system. *Journal of Structural Geology, 20*(7), 865-881. https://doi.org/10.1016/S0191-8141(98)00023-6

Sibson, R. H. (1996). Structural permeability of fluid-driven fault-fracture meshes. *Journal of Structural Geology, 18*(8), 1031-1042. https://www.doi.org/10.1016/0191-8141(96)00032-6

Sillitoe, R. H. (2010). Porphyry copper systems. *Economic Geology, 105*, 3-41. https://doi.org/10.2113/gsecongeo.105.1.3

Simmons, S. F., White, N. C., & John, D. A. (2005). Geological characteristics of epithermal precious and base metal deposits. *Economic Geology 100th Anniversary Volume*, 485-522. https://doi.org/10.5382/AV100.16

Siratovich, P. A., Heap, M. J., Villeneuve, M. C., Cole, J. W., & Reuschle, T. (2014). Physical property relationships of the Rotokawa Andesite, a significant geothermal reservoir rock in the Taupo Volcanic Zone, New Zealand. *Geothermal Energy, 2*(10), 31. https://doi.org/10.1186/s40517-014-0010-4

Slemmons, D. B. (1957). Geological effects of the Dixie Valley-Fairview Peak, Nevada, earthquakes of December 16, 1954. *Bulletin of the Seismological Society of America, 47*, 353-375.

Solum, J. G., Davatzes, N. C., & Lockner, D. A. (2010). Fault-related clay authigenesis along the Moab Fault; implications for calculations of fault rock composition and mechanical and hydrologic fault zone properties. *Journal of Structural Geology, 32*(12), 1899-1911. https://doi.org/10.1016/j.jsg.2010.07.009

Sornette, D. (1999). Earthquakes: from chemical alteration to mechanical rupture. *Physics Reports, 313*(5), 237-292. https://doi.org/10.1016/S0370-1573(98)00088-X

Speed, R. C. (1976). Geologic map of the Humboldt Lopolith and surrounding terrane, Nevada. The Geological Society of America, Map and Chart Series MC-14. 1:80,000.

Speed, R. C., & Jones, T. A. (1969). Synorogenic quartz sandstone in the Jurassic Mobile Belt of western Nevada: Boyer Ranch Formation. *Geological Society of America Bulletin, 80*, 2551-2584. https://doi.org/10.1130/0016-7606(1969)80[2551:SQSITJ]2.0.CO;2

Summers, R., Winkler, K., & Byerlee, J. (1978). Permeability changes during the flow of water through Westerly Granite at temperatures of 100-400°C. *Journal of Geophysical Research, 83*(B1), 339-344. https://doi.org/10.1029/JB083iB01p00339

Swanson, P. L. (1984). Subcritical crack growth and other time- and environment-dependent behaviors in crustal rocks. *Journal of Geophysical Research, 89*(B6), 4137-4152. https://doi.org/10.1029/JB089iB06p04137

Thompson, G. A., Meister, L. J., Herring, A. T., Smith, T. E., Burke, D. B., Kovach, R. L., et al. (1967). *Geophysics, study of Basin-Range structure, Dixie Valley region, Nevada. U.S. Air Force Cambridge Research Labs. Spec. Rept. 66-848.*

Tosdal, R. M., Dilles, J. H., & Cooke, D. R. (2009). From source to sinks in auriferous magmatic-hydrothermal porphyry and epithermal deposits. *Elements, 5*(5), 289-295. https://doi.org/10.2113/gselements.5.5.289

USGS & NBMG. (2010). Quaternary fault and fold database for the United States. Retrieved from https://earthquake.usgs.gov/hazards/qfaults/

Vikre, P. G. (1993). Gold mineralization and fault evolution at the Dixie Comstock Mine, Churchill County, Nevada. *Economic Geology, 89*(4), 707-719. https://doi.org/10.2113/gsecongeo.89.4.707

Wallace, R. E. (1984). Patterns and timing of Late Quaternary faulting in the Great Basin Province and relation to some regional tectonic features. *Journal of Geophysical Research - Solid Earth, 89*(B7), 5763-5769. https://www.doi.org/10.1029/JB089iB07p05763

Wallace, R. E., & Whitney, R. A. (1984). Late Quaternary history of the Stillwater Seismic Gap, Nevada. *Bulletin of the Seismological Society of America, 74*(1), 301-314.

Watters, R. J., Zimbelman, D. R., Bowman, S. D., & Crowley, J. K. (2000). Rock mass strength assessment and significance to edifice stability, Mount Rainier and Mount Hood, Cascades Range volcanoes. *Pure and Applied Geophysics, 157*, 957-976. https://doi.org/10.1007/s000240050012

Whitney, D. L., & Evans, B. W. (2010). Abbreviations for names of rock-forming minerals. *American Mineralogist, 95*(185-187), 185-187. https://www.doi.org/10.2138/am.2010.3371

Wilkins, J. S. (1980). Slow crack growth and delayed failure of granite. *Int J Rock Mech Min Sci & Geomech, 17*, 365-369. https://doi.org/10.1016/0148-9062(80)90520-3

Williams, D. P., & Evans, A. G. (1973). A simple method for studying slow crack growth. *JTEVA, 1*(4), 264-270. https://doi.org/10.1520/JTE10015J

Williams, J. N., Toy, V. G., Massiot, C., McNamara, D. D., & Wang, T. (2016). Damaged beyond repair? Characterising the damage zone of a fault late in its interseismic cycle, the Alpine Fault, New Zealand. *Journal of Structural Geology, 90*, 76-94. https://doi.org/10.1016/j.jsg.2016.07.006

Wilson, J. E., Chester, J. S., & Chester, F. M. (2003). Microfracture analysis of fault growth and wear processes, Punchbowl Fault, San Andreas system, California. *Journal of Structural Geology, 25*, 1855-1873. https://doi.org/10.1016/S0191-8141(03)00036-1

Wyering, L. D., Villeneuve, M. C., Wallis, I. C., Siratovich, P. A., Kennedy, B. M., Gravley, D. M., & Cant, J. L. (2014). Mechanical and physical properties of hydrothermally altered rocks, Taupo Volcanic Zone, New Zealand. *Journal of Volcanology and Geothermal Research, 288*, 76-93. https://doi.org/10.1016/j.jvolgeores.2014.10.008

Yasuhara, H. (2005). Fault zone restrengthening and frictional healing: The role of pressure solution. *Journal of Geophysical Research, 110*(B6). 10.1029/2004jb003327